Dynamics of an actin spring: The acrosomal process in the *Limulus polyphemus* sperm

by

Jennifer Hyunjong Shin

B.S., Mechanical Engineering (1998)

Massachusetts Institute of Technology

Submitted to the Department of Mechanical Engineering
in partial fulfillment of the requirements for the degree of
Master of Science in Mechanical Engineering
at the
MASSACHUSETTS INSTITUTE OF TECHNOLOGY
September 2000

Author .....
Department of Mechanical Engineering
August 4, 2000

Certified by .....
L. Mahadevan
van Tassel Associate Professor of Mechanical Engineering
Thesis Supervisor

Certified by .....
Paul Matsudaira
Professor of Biology, Bioengineering and Environmental Science
Thesis Supervisor

Accepted by .....
Ain A Sonin
Chairman, Department Committee on Graduate Students
Department of Mechanical Engineering

Dynamics of an actin spring: The acrosomal process in the *Limulus polyphemus* sperm

by

Jennifer Hyunjong Shin

Submitted to the Department of Mechanical Engineering
on August 4, 2000, in partial fulfillment of the
requirements for the degree of
Master of Science in Mechanical Engineering

Abstract

We study the dynamics of the acrosomal process in the sperm of the horseshoe crab, *Limulus polyphemus*. In its native state, the acrosomal bundle consists of a 60μm para-crystalline helical coil of bent, twisted actin filaments. In the presence of Ca^{2+}, the actin binding protein, scruin, undergoes a conformation change, which causes the individual actin filaments to untwist. This leads to the straightening of the 60μm long bundle which is propelled through a nuclear channel at a mean velocity of 15μm/s at room temperature (24-26^{o}C). Its velocity is constant throughout the entire extension, suggesting that the uncoiling of the bundle is a localized event that propagates in a zipper-like fashion. The average velocity of the acrosomal process depends on the temperature and increases as the temperature is raised, varying from approximately 37μm/s at 32^{o}C to 1.7μm/s at 9.6^{o}C. The morphological dependence in the reaction rate was investigated by electron micrograph studies, and the effects of external load was also studied by varing the viscosity of the medium through which the acrosomal bundle extends. Results indicate no morphological dependence on the reaction rate but the viscosity of the medium exhibited a negative correlation with the extension velocity. Based on dynamical measurements of the uncoiling and the extension of the actin bundle, we estimated the energy dissipated hydrodynamically during the extension to be of the order of 10^{-8}ergs. The bending stiffness, EI, of the actin bundle was measured by analyzing the bending shape at equilibrium in a steady hydrodynamic flow and was of the order of 10^{-20}Nm^2 leading to an estimate for the initially stored energy of $7{\cdot}10^{-6}$ergs. Therefore, the acrosomal bundle indeed behaves like a mechanical spring, and the strain energy is the major source of the energy that powers the acrosomal reaction to completion.

Thesis Supervisor: L. Mahadevan
Title: van Tassel Associate Professor of Mechanical Engineering

Thesis Supervisor: Paul Matsudaira
Title: Professor of Biology, Bioengineering and Environmental Science

Acknowledgments

First of all, I would like to thank Professor L. Mahadevan and Professor Paul Matsudaira for offering me a great opportunity to work for them and introducing me this spectacular problem in biophysics presented in this thesis. For last two years, they have been guiding and supporting my research with consistent trust and encouragement. I thank both my advisors for their sincere advice of independence and self-confidence in my thoughts and actions. They patiently waited and guided me while I was making my rough entrance to the field of biophysics with my limited background.

It has been a great pleasure to work with people in the Matsudaira Lab at the Whitehead Institute. I first thank Guichy Waller and Nicki Watson for their kind help in experiments and their encouragement and advice during my hard moments. They were the first two people from the Whitehead Institute who patiently helped me make my tumble entrance to biological experiments. I thank Jeff Chiou and Sung Choe for their kinds words and concerns. Ivan Correia, James Evans, Yelena Freyzon, Anya Goodmand, and Joan Zhong were so kind and patient with this inexperienced Mechanical engineer working in a biology lab as to spare their time and effort to help me and guide me out of my ignorance. I also thank Ms. Julie Ellis and Anna Dunavin for their friendly assistance with administrative matter.

I am also grateful to everyone in the Mechanics and Materials group, Tom Arsenlis, Kevin Bass, Mats Danielsson, Heather Dunn, Brian Gearing, Jeremy Gregory, Sauri Gudlavalleti, Fatima Haq, Jinchul Hong, Rami Rokas, Greg Nielson, Ethan Parsons, Hang Qi, Yu Qiao, Cheng Su, Prakash Thamburaja, Steve, Xia, Jin Yi , and Ting Zhu. Their friendship, care, and their willingness to help in all possible issues made my average sixteen hour stay in my office very pleasant and comforting. Especially, Jinchul Hong, who is like a brother in heart, shared hardships and laughs with me for last two years. Mr. Ray Hardin was always so nice as to listen to my problems and help me fix them even in his busiest moments.

I would also like to send warmest regard and appreciation to my friends who supported me for last two years. Very special thanks go to Dr. Ho-Young Kim who always encouraged and helped me in my lowest moments. His sincere care, funny jokes, harsh advice, and faithful love made it possible for me to continue and not give up when I tumbled down

exhausted. I thank my dearest friends Heather Koh and Alice Oh (and her husband, Tae-sik Lee) for being good friends and for cooking me delicious and nutritious dinners to help me keep going.

My thanks go to Ms. Leslie Regan for her excellent administrative assistance and for patiently waiting for this thesis to be finalized.

Finally, last but not least, I would like to acknowledge my parents with my greatest thanks and love. I also send my love and thanks to my wonderful sisters, brothers-in-law, and my nine dearest nephews and nieces including the youngest one to be born in March 2001.

Contents

List of Figures

List of Tables

Chapter 1

Introduction

1.1 Background and motivation

1.1.1 What is the acrosomal reaction (AR) of *Limulus polyphemus* sperm

The acrosomal reaction is an essential step that precedes fertilization in animals. In most marine invertebrates, it is often a coupled reaction of exocytosis (rupturing of the acrosomal vesicle) and a dramatic morphological change (formation of the acrosomal process) [53]. At fertilization when the sperm cells make contact with the jelly coat of an egg, the acrosomal reaction is activated. Upon activation, the acrosomal vesicle ruptures, and a needle-like process is extruded from the head of the sperm following the release of lytic enzymes (See Fig. 1-1 and 1-2). This needle is termed the acrosomal process which bridges the gap between the sperm and the egg plasma membrane, and starts the physical process of fertilization.

Despite the common biological purpose of the acrosomal reaction, the mechanism employed varies with species. In many Echinoderms, a phylum that includes sea urchins, sea cucumbers, and sea stars, the acrosomal process is formed from subacrosomal precursors, namely actin monomers, during the acrosomal reaction. For instance, in the sperm of *Thyone* (sea cucumber) the actin bundle assembles by polymerization of actin monomers stored in a sac. In unreacted sperms, the actin monomers are

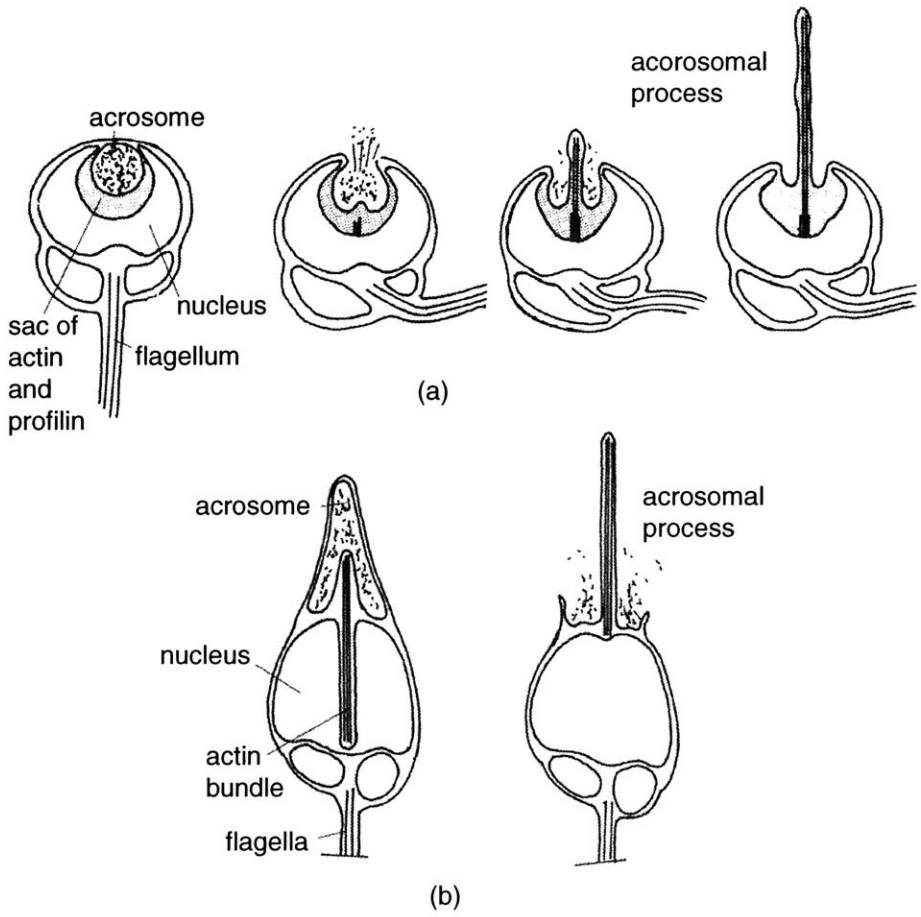

Figure 1-1: (a) Acrosomal Reaction in *Thyone* sperm. Size of the sperm head is about 5μm in its diameter. The length of 90μm actin bundle can be polymerized in less than 10 seconds. (b) *Mytilis* sperm acrosomal reaction. The 6-7μm bundle of about 50 preformed actin filaments is extruded out to completion in few minutes [3].

cross-linked with a protein called profilin which prevents the actin monomers from polymerizing. Upon activation, profilin falls off, and the actin monomers begin to polymerize to form a long acrosomal process made of actin [3] (See Fig.1-1(a)).

In contrast to polymerizing mechanism, in a bivalve mollusk (*Mytilus*) and an arthropod (*Limulus*), a filament structure is preformed and present in the mature unreacted sperm [22, 25, 38, 54]. The extension mechanism in these species are fundamentally different from the polymerization mechanism as their acrosomal bundle is preformed during the development (See Fig.1-1(b)). The preformed acrosomal process found in *Mytilus* is a straight rod (6-7μm) which are extruded upon activation.

In this thesis, we will concentrate on the acrosomal process of *Limulus* sperms

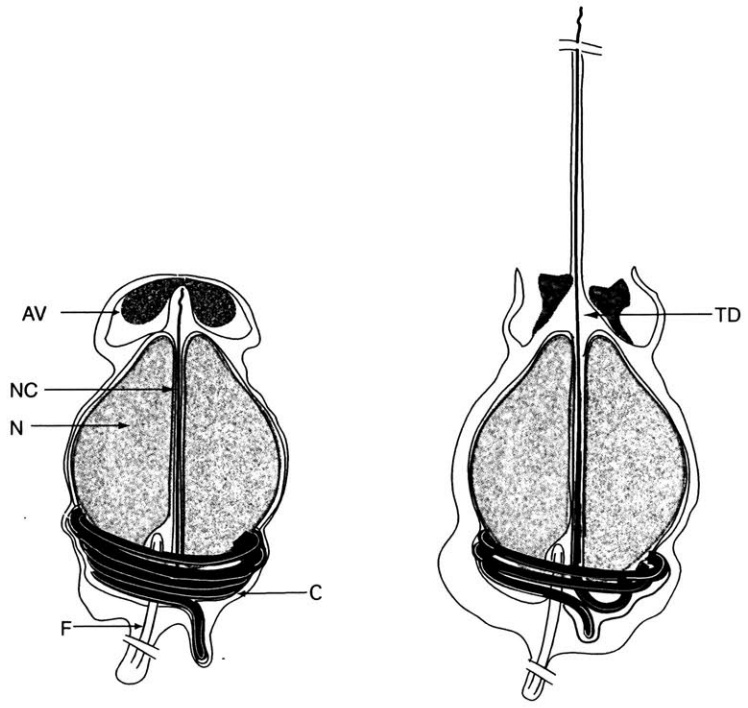

Figure 1-2: Acrosomal reaction in *Limulus* sperm. In native state, the anterior end of the bundle lies inside the nuclear channel (NC) while the posterior end exists as a coil with 5-6 loops (C). Once activated either by Ca^{2+} or by the presence of an egg, the acrosomal bundle gets extruded out of the nuclear channel to penetrate itself into the egg. An average size of the sperm head is about 4μm wide and 5μm long, and a typical velocity of the reaction is about 15μm/s. AV: acrosomal vesicle, N: nucleus, F: flagellum, and TD: true discharge.

which features a very unique and complex morphology of the preformed acrosomal bundle. Its transformation during the acrosomal reaction is also unique, and involves a considerable degree of complexity. Brown (1976) suggested that the complexity in the structure may be related to the difficulty of penetrating the tough surface coats of the *Limulus* egg. As shown in Fig. 1-2, in its native state, the proximal end of the bundle lies in a channel through the nucleus while the distal end, surrounded by the nuclear membrane, is coiled around the base of the nucleus, making about 6 loops. In the presence of Ca^{2+} or when the sperm encounters an egg, the initially coiled bundle uncoils into a 60μm long, straight bundle called the true discharge(TD) in a few seconds.

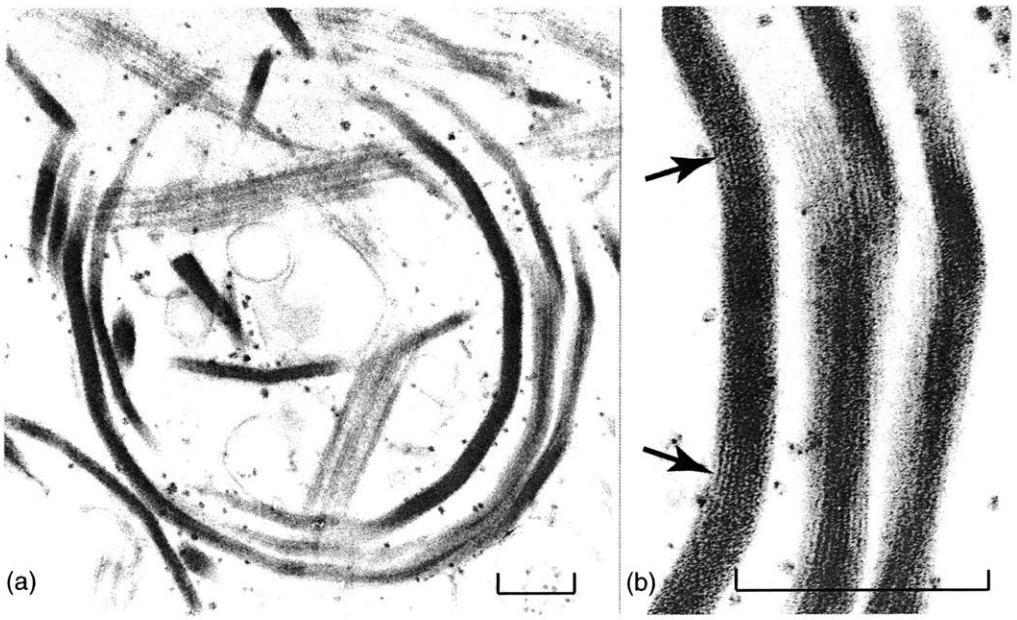

Figure 1-3: Thin section of the coil: Coils were purified by treating the *Limulus* sperm with glycerol and Triton X 100 along with several centrifugation. (a) The thin section cut across the coil from the unreacted sperm indicates that it has 14 elbows and 15 straight segments per one loop of coil. (b) The arrow indicates the elbows at 156°. Both scale bars measure 0.5μm [10]

1.1.2 How does the AR happen?

The acrosomal reaction of the *Limulus* sperm is of interest as it involves a novel mechanism of force generation for the reaction to occur. While force production at the molecular level is typically associated with the ATP(Adenosine triphosphate) hydrolysis or myosin, the acrosomal reaction in *Limulus* sperm does not involve any of ATP, myosin, or actin polymerization. The bundle starts out as a bent and twisted coil, and extends out to form a long, straight bundle during the reaction. Force generation involves only a structural reorganization of preexisting components in the *Limulus* sperm, and is thus akin to what happens when a compressed spring is released.

To understand the microscopic mechanism of the acrosomal process, we start with a description of the structure of the bundle using the electron micrographs of DeRosier and Tilney (See Fig. 1-3). In its native state, the acrosomal bundle consists of a paracrystalline array of bent and twisted actin filaments. In the coil, the actin

bundle is a right handed superhelix: for each loop of coil (there are 6 loops in the coil), the bundle has 2.3 turns around its axis [10]. Due to this feature, one can expect the extending bundle to make 2.3 revolution per loop of the coil discharged, and in fact this rotational motion is observed in the presence of a kink at the tip of the bundle (see Fig. 1-4). The bundle features 14 arms and 14 elbows per each loop of the coil (See Fig. 1-3). These elbows are thought to have been introduced by the differential sliding between the actin filaments. In passing through an elbow, each actin filament experiences difference in its path length. Since no compression or extension of the filaments were observed in the bundle, there must be some slippage between actin filaments relative to one another. Having a 60° superhelicity in the bundle and the 156° angle of each elbow ensures that 1) the filaments passing through the elbow cover the equal path length for neighboring filaments to form crossbridges on both sides of elbow, and 2) there is no indefinite accumulation of slippage along the filaments but an oscillating feature of slippage and crossbridges [9].

In addition to the superhelicity of the bundle, each filament is slightly over-twisted by 0.23° per subunit. Actin filaments in their unbound form can have about 5-6° angular disorder per subunit [12], which helps to explain the presence of overtwisting in the acrosomal bundle in *Limulus* sperm. Since actin subunits are added at their membrane-associated end during spermatogenesis [55], the "modest fluctuations in the twist of actin subunits are captured and frozen-in by scruin" [34], and the degree of twist in the *Limulus* bundle is well within the range of their random variable twist [13]. This overtwisting of the actin filaments causes stress on the filaments. DeRosier and Tilney proposed that this feature store elastic strain energy in the coil [8]. During the uncoiling process, the untwisting of the bundle is accompanied by slippage between filaments and untwisting of the individual actin filaments, leading to the conversion of the coil to its straight form. In doing so, mechanical potential energy stored in the coil is converted into translational work, as in a mechanical spring. Once the reaction is finished, the actin bundle lies in its lower energy state than that of its coiled state, and as a result, the true discharge reaction cannot be reversed.

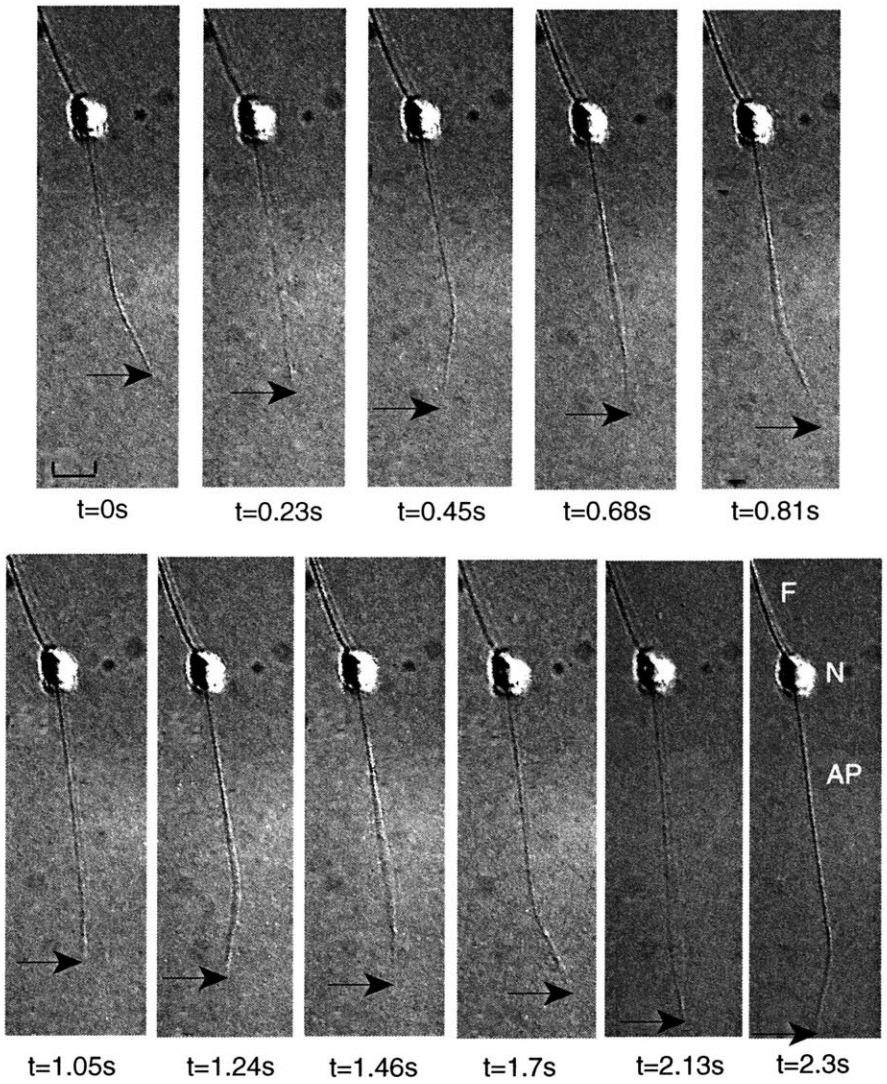

Figure 1-4: A sequence of selected frames of the acrosomal process. As shown in the images, there exists a kink at the tip of the bundle and the orientation of the kink flips left to right during the reaction. This suggests that the bundle rotates as it elongates. During one revolution of the bundle, the tip advances by $\sim 4.3\mu$m. The arrow indicates the location of the tip. F: flagellum, N: nucleus or sperm head, AP: acrosomal process. Scale bar measures 5μm.

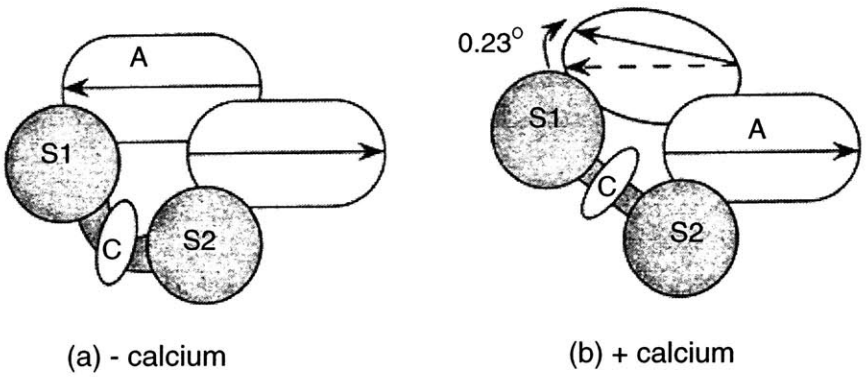

Figure 1-5: Scruin consists of a calmodulin (C) and two domains, S1 and S2, and the calmodulin lies in the neck region of the two domains. Scruin lies across the actin (A) filament axis and is bound to actin through two separate domains. When calcium binds to CaM changing the binding affinity to scruin, two domains of the scruin change their orientation which allows space for actin filaments to untwist by 0.23° per subunit. [46].

What is then happening at the molecular level during the acrosomal reaction? The acrosomal process has two major components, actin and an actin crosslinking protein, scruin. To characterize its actin binding properties, native scruin was purified by Sanders et al (1996) using HECAMEG (methyl-6-*O*-(*N*-heptyl-carbamoyl)-α-D-glucopyranoside) detergent extract with high calcium. They identified the scruin as an equimolar complex with calmodulin. Scruin consists of two domains (S1 and S2 in the Fig.1-5 represents N- and C- terminal domains of scruin) and calmodulin(CaM) which lies in the neck region of the two domains. Scruin lies across the filament axis and is bound to actin through two separate domains. While one domain of scruin crosslinks with one subunit of an actin filament, the other domain of scruin binds to other subunit of the same filament. Their I-Calmodulin overlays and calmodulin-Sepharose indicated that scruin binds calmodulin in calcium but not in EGTA (egtazic acid, a calcium chelating agent), and that calcium alters scruin conformation.

The presence of calmodulin and the conformational dependence of scruin on calcium immediately suggest us that calcium be the intracellular signal to trigger or drive the acrosomal reaction. Scruin crosslinking to actin, however, was found to be independent of the presence of calcium. In other words, the uncoiling does not involve an on-off actin binding mechanism but only a conformational change in scruin, which

further influences the conformation of its neighboring actin filaments [46].

Based on these results, they were able to hypothesize that a change in twists of the actin filaments is caused by scruin, calcium, and calmodulin. Binding of calcium to CaM changes the CaM binding affinity to the neck region of the scruin and thus shifts the orientation of the scruin domains. Minute changes in scruin conformation are then transmitted to the bound actin subunits which allows the actin filaments to untwist by 0.23° between subunits [10, 8]. As the filaments untwist, the scruin-scruin crosslinks between neighboring filaments break transiently to allow the slippage between them. Sherman et al. (1999) found a variety of non-identical contacts between scruin subunits and filaments from the crystallographic reconstruction. This variety of interactions permits filaments to remain bundled while undergoing the slippage and changes in twist with respect to one another [48]. The local change in twist is then magnified through mechanical coupling along the entire length of the bundle (approximately 10^6 subunits for the entire bundle), leading to uncoiling and extension of a 60μm long structure to penetrate into the coating of the egg. On the other hand, the energy released from the unbending events of the kinks by differential sliding of the filaments is energetically not dominant (See chapter 3.2) [34].

1.1.3 Why the AR in *Limulus* sperm?

As briefly mentioned above, the force generation involved in the acrosomal process is not achieved by ATP or any other known molecular motor mechanism. This mechanism only involves a structural reorganization of a preexisting actin bundle and the actin binding proteins while initially stored mechanical potential energy in the coil state of the bundle is converted into translational work. As this involves not only biochemical reactions but also mechanical conversion of a coil into a straight bundle, understanding dynamics of the reaction is crucial. Recent advances in high precision experimental techniques such as optical tweezers, magnetic traps, high resolution video-microscopy, atomic force microscopy, and other similar techniques have made it possible to study the non-equilibrium mechanics at a single-molecule level. Based on the knowledge on its function and structure, it now offers a good opportunity

for a dynamic analysis with both experimental studies and theoretical modeling at a biophysical level.

Understanding of this spring-like extension of the acrosomal process can be enormously powerful since this reaction has every potential to be a generic mechanism to approach other systems that involve molecular springs. Furthermore, we may be able to explain other, yet unknown, actin-based motilities which do not involve ATP, myosin, or actin-polymerization.

1.2 Objectives

The mechanism of the acrosomal reaction in *Limulus* sperm cannot be explained with any conventional models of actin-based motility. Our primary goals are to determine the mechanism of the uncoiling process and to quantify the energy involved in the entire reaction. In particular, we are interested in the mechanism of energy storage and release, and if it is indeed associated with the bending and twisting of the filaments. This work combines experiments and analytical studies to estimate energetics of the acrosomal reaction.

1.3 Organization of thesis

The present chapter describes the background, motivation, and objectives of this study. Chapter 2 begins by considering various uncoiling mechanisms of the acrosomal process and showing how a particular mechanism is consistent with the results from the experiments. Effects of temperature, morphology, and viscosity on the reaction rate are discussed in detail in the rest of chapter 2. In chapter 3, the energy involved in the reaction is analytically estimated by considering the initially stored potential energy, the hydrodynamic dissipation, and calcium binding energy released during the extension. Chapter 4 explains an experimental method of measuring the bending stiffness of the acrosomal bundle, namely a steady deflection method. This involves the hydrodynamic flow of a known velocity to deflect the bundle. Chapter 5 offers the conclusions of this thesis with suggested future works.

Chapter 2

Acrosomal reaction in the *Limulus* sperm

2.1 Global or local uncoiling?

We start our investigation by identifying various mechanism of the uncoiling in the acrosomal process. As discussed in chapter 1, in its native state, the acrosomal bundle features a superhelical coil of 15-80 twisted actin filaments latched by scruin molecules. When Ca^{2+} binds to calmodulin which lies in the neck region of scruin, the scruin molecules undergo conformational change, leading to untwisting of individual actin filaments. As the actin filaments untwist, the bundle uncoils to form a 60μm straight actin bundle. Two extreme scenarios of a mechanism are as follows. The first mechanism is a global explosion model which involves simultaneous uncoiling of the bundle, with the nuclear channel converting the change into the motion. The second mechanism is an unzipping model where a spatially localized zone of conformational change separates the two states of acrosome, namely coiled and uncoiled, so that only a segment of the bundle uncoils at any one incident of time. This model is similar to transitions in crystalline materials such as metals. In this scenario, there will be an incremental energy release per each unlocking event of scruin, which causes the bundle to lengthen at a nearly constant velocity.

These two mechanisms for the extension of *Limulus* acrosome can be distinguished by analyzing its extension profile in time. For the case of the global explosion model, a decrease in velocity with time is expected after a short initial explosive transition.

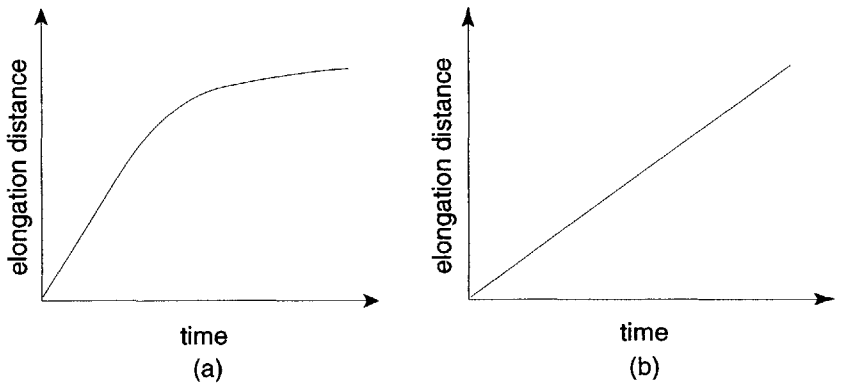

Figure 2-1: Expected extensino profile in time for two possible uncoiling mechanism. (a) is for the global explosion mechanism where the increment of elongation distance decreases in time due to the decrease in the reaction rate. (b) correspond to the constant velocity reaction where the extention profile is linear in time.

The localized mechanism leads to a nearly constant force and velocity throughout the reaction due to the incremental conformation change. (See Fig. 2-1).

2.1.1 Experimental setup and procedure

Collecting and washing sperm sample

Limulus polyphemus, horseshoe crabs, were supplied by the Marine Biological Laboratory at Woods Hole, Massachusetts. Sperms of the horseshoe crab (500μl) were collected into a 1.5 ml polypropylene tube by applying mechanical stimulation to one selected crab, *i.e.*, by rubbing gently near its gonapores. When this mechanical method fails, a 9 V battery was used on their flap to give them a brief electric shock [52]. Collected sperms were washed twice in artificial sea water (ASW) by spinning at 82g for 1 min in Eppendorf tabletop microfuge. ASW is made of 9.27mM $CaCl_2$, 423mM NaCl, 22.94mM $MgCl_2$, 25.5mM $MgSO_4$, 2.15mM $NaHCO_3$, 9mM KCl and 10mM Tris at pH 8, and the pH of the buffer is adjusted to 7.8 to 7.9. The washed pellet was resuspended in ASW to its original volume and kept on ice at all times. If the collected sperm were not used immediately, sperms may be stored at 4°C as a concentrated form. Sperms usually remain healthy for a couple of days at 4°C. Once frozen, sperms do not undergo the acrosomal reaction even in the presence of excess calcium when thawed. Collected sperms and all the buffers used in the experiment

were kept on ice at all times unless otherwise specified.

Capillary flow cell

A flat capillary flow cell ($\sim$ 30μl: 18mm x 6mm x 0.3mm (length x width x depth)) was made from two coverslips (Corning, Corning, NY) to allow easy perfusion and to prevent rapid evaporation. The flow cell was assembled on a piece of clean lens paper that is free of dirt and oil. First, a coverslip (50mm x 24mm (length x width)) was cut in small pieces (24mm x 5mm) with a diamond knife to be used as supporting legs. On an uncut coverslip, two thin tracks of vacuum grease (Epiezon) was applied along each of the long side of the coverslip by using a syringe fitted with a 24G-gauge needle. The spacing between the tracks of the grease was carefully done for each flow cell so that the sample volume is consistent for all flow cells. On each of the vacuum grease tracks, two supporting legs were placed. On the top of the legs, another lines of grease were applied for a round coverslip (18mm diameter) to sit on.

The capillary flow chamber was made for two reasons. First, it makes it easier to perfuse calcium ionophore, calcium, and ASW to adjust to the condition and sperm concentration optimal for experiments. Secondly, having an enclosed chamber keeps the sample from drying out.

Acrosomal reaction velocity measurements

1 μl of the washed sperm sample was diluted in 1 ml of 25 mM $CaCl_2$ in artificial sea water (ASW). Since the concentration of the sperm sample varies considerably depending on the crabs and their conditions, dilution must be varied from sample to sample. With 100X objective and 10X eyepiece, it is desired to have 5$\sim$10 sperms per field of microscope view. Before adding sperm cells into the chamber, 30 μl of ASW was added. This step reduces the number of sperms sticking on the surface of the coverslips. 30 μl of the diluted sperm sample was then perfused into the flow cell while excess liquid was drawn from the other side of the chamber. Calcium ionophore A23187 (1mg/ml in dimethyl sulfoxide(DMSO)) was diluted 1:10 in 25 mM $CaCl_2$ in ASW. 10μl of the diluted A23187 was then pipetted into the flow cell to induce

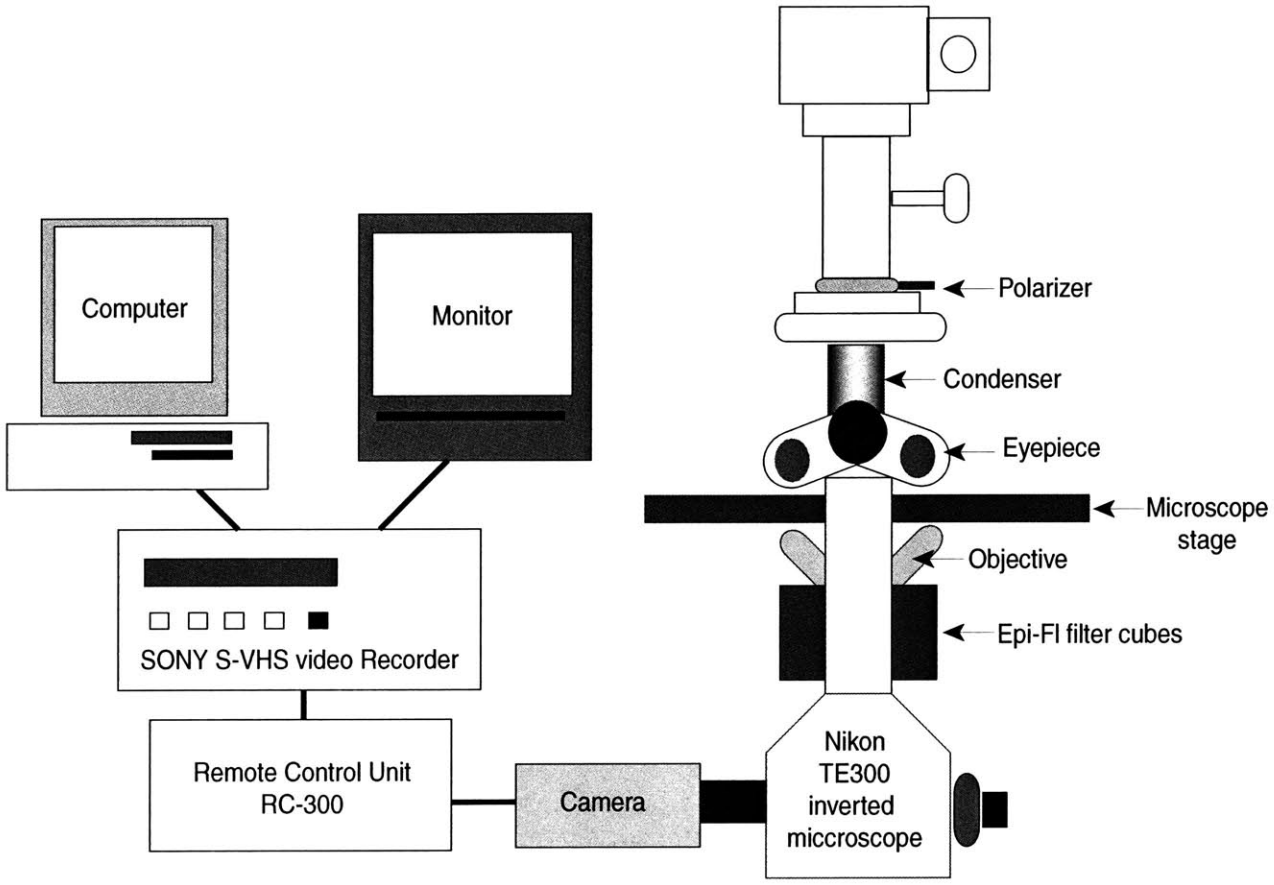

Figure 2-2: A schematic of experimental setup for the imaging of the acrosomal reaction.

the true discharge. Again, excess liquid was drawn out from one side of the flow cell while the ionophore was being pipetted into the other side.

Light microscopy, recording, and digitizing

As ionophore diffuses in the flow cell, sperms begin to react. The reactions were observed with Nikon Eclipse TE300 inverted microscope equipped with a Nikon plan apo-100X DICH (Differential Interference Contrast) oil immersion objective lens (numerical aperture (N.A.) 1.4), 10X CFI eyepiece, and a LWD condender. Images were acquired with a Hamamatsu CCD (Charged Coupled Device) video camera (Model C2400-35), and video-taped simultaneously with a Sony S-VHS video cassette recorder at 30 frames per second (See Fig.2-2). Video images of selected acrosomal reactions were digitized at a video rate using an Apple Video Player (Apple computer, Inc). At the end of each experiment, the image of a stage micrometer was also

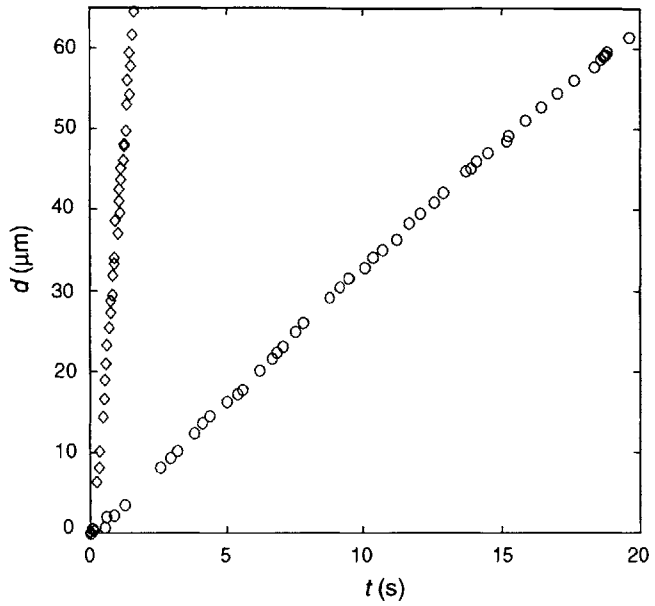

Figure 2-3: Elongation (d)-time (t) relationship in *Limulus* acrosomal process. The evolution of the acrosomal process was followed quantitatively using video microscopy. The diamonds represent the fastest elongation profile with its velocity of 37 μm/s at 32°C while the open circles represent one of the slowest (1.7μm/s) at 9.6°C. Despite the variations in velocities with temperature, each reaction displays a constant velocity profile over the entire extension period.

recorded and digitized as a PICT file to be used for calibration.

Data analysis

The digitized images of each reaction were saved as movie files and replayed using an image analysis software GYROSCOPE kindly provided by Dr. Hugo Ayala from Department of Mechanical Engineering at MIT. This software allows us to play the movie frame by frame, measure the elongation and simultaneously create a data file with the measurements from each frame. The calibrated measurements lead to the elongation which is plotted as a function of time using MATLAB.

2.1.2 Results and discussions

Uncoiling mechanism

The plot of elongation versus time shows that the acrosome extends with a constant velocity (See Fig.2-3). Although there were variations in the velocity observed from

one sperm cell to another, in each case the velocity was constant over time. This result is consistent with the second mechanism associated with the unzipping model.

On a microscopic scale, the conformational change in the actin-crosslinking protein scruin probably leads to the untwisting of the actin filaments. This is a spatially localized event and there is an incremental energy release that powers the extension. If enough actin filaments are untwisted, the reaction proceeds spontaneously, much as a defect propagates through a crystal once it is set in motion. From both a structural and an energetic viewpoint, it is much easier for a zone of localized conformation change in the filaments to propagate along the coiled bundle, as in the crystals.

Variations in the data

Factors that may contribute to the variation in the extension rate include a spatially inhomogeneous distribution of Ca^{2+} or ionophore, the condition of crabs, the individual difference among sperm cells, and freshness of the collected sperm samples. In addition, most of sperms videotaped were located near the surface of the coverslip, and thus the proximity of the sperms to the surface could be one of the factors. Depending on the distance of the sperm from the surface, the moving acrosomal bundle experiences different shear forces, which in turn may affect the velocity of the extension.

2.2 Temperature dependence on the acrosomal reaction rate

In many biological systems, it is often found that the rate of the reaction depends on the temperature at which the reaction occurs. In the case of the temperature dependence for the relaxation rate of a mammalian muscle twitch, the changes in the rate constant for Ca^{2+} binding to troponin affect the relaxation rate since the rate constant for the chemical reaction is related to temperature by an Arrhenius equation [49]. Ca^{2+} also plays a significant role in the acrosomal reaction and thus the rate of Ca^{2+} binding to calmodulin and consequent conformation changes in calmodulin, scruin, and actin filaments may also exhibit similar dependencies on temperature. In

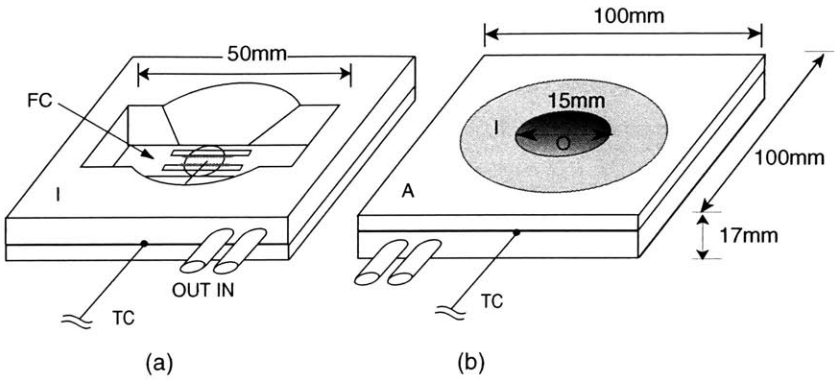

Figure 2-4: (a) Top view of the temperature controlled substrate: there is a pocket for a flowcell(FC) to fit in. To allow space for the condenser to move up and down, the pocket is gradually indented with enough space to make sample loading and withdrawing easy. The upper unit has an inlet and an outlet for water circulation inside the substrate made of aluminum(A). (b) Bottom view: 5mm thick insulator(I) (made of G10) of a circular shape (75mm in diameter) is attached to the bottom of the substrate so that the substrate would fit into a microscope stage and an opening(O) of 30mm diameter was machined for objectives. A narrow groove was made on the upper side of the bottom unit in such a way that the thermocouple(TC) can be inserted through between the upper and lower units. The schematics are not drawn to scale.

this section, the effect of temperature on the acrosomal reaction rate is investigated.

2.2.1 Experimental setup and procedure

Temperature controlled stage and flow cell

In order to have a precise control over temperature in our experiment, a temperature controlled stage was designed. The stage is made of aluminum and consists of two parts. The lower part is a 100mm x 100mm x 5mm plate machined such that its one side would fit in the circular hole in the microscope stage (See Fig. 2-4 (b)). The other side of the lower plate has a 50mm x 25mm x 2mm pocket to place a flow cell. The upper unit is a 100mm x100mm x 12mm hollow unit with an inlet and an outlet for water circulation (Fig. 2-4 (a)). The two parts of the stage were hinged to allow easy opening and closure of the device for mounting and removal of a flow cell. The temperature-controlled stage was insulated with a polymeric material, leaving a circular opening of 30mm diameter both on the top and the bottom to

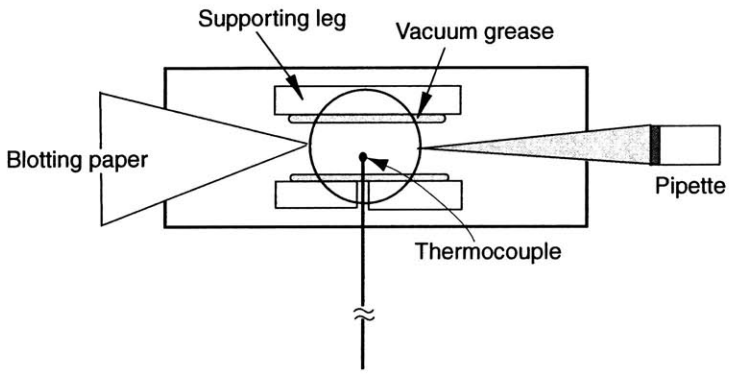

Figure 2-5: Flowcell used for the temperature dependence experiment.

accommodate the condenser and the objective, respectively. The temperature of the substrate is regulated by influx and outflow of heated or chilled water from a VWR-1165 temperature regulator.

Due to the presence of a large heat sink in the path from the heated water in the circulator to the sample, the actual temperature of the sample inside the flow cell could be raised only upto $\sim 35°C$ when the water circulator is set at 90° C. For effective cooling, a cooled air jet was blown directly to the flow chamber from the bottom side of the flow cell. One end of a PVC tubing (1/2 inch innder diameter) was connected to an air jet on the wall, and the mid region of the tube was passed through a liquid nitrogen container. The tubing was then used to wrap the objective which is in contact with the flow cell. The open end of the tube was situated so that the cooled air would be blown directly on the bottom side of the flow cell. By controlling the air flux and the heating/cooling feature of the water bath, sample temperature was effectively lowered down to $4°C$.

An Omega digital thermometer HH-21 was used to monitor the temperature from a thermocouple (typeK, Omega) mounted between the two coverslips of the modified flow cell to allow space for thermocouple. This arrangement provided an accurate measurements of temperature inside the flow cell during the experiment. Fig.2-6 is the control and its measurement. Videomicroscopy setup is identical with the one described in section (2.1.1) (See Fig.2-2)

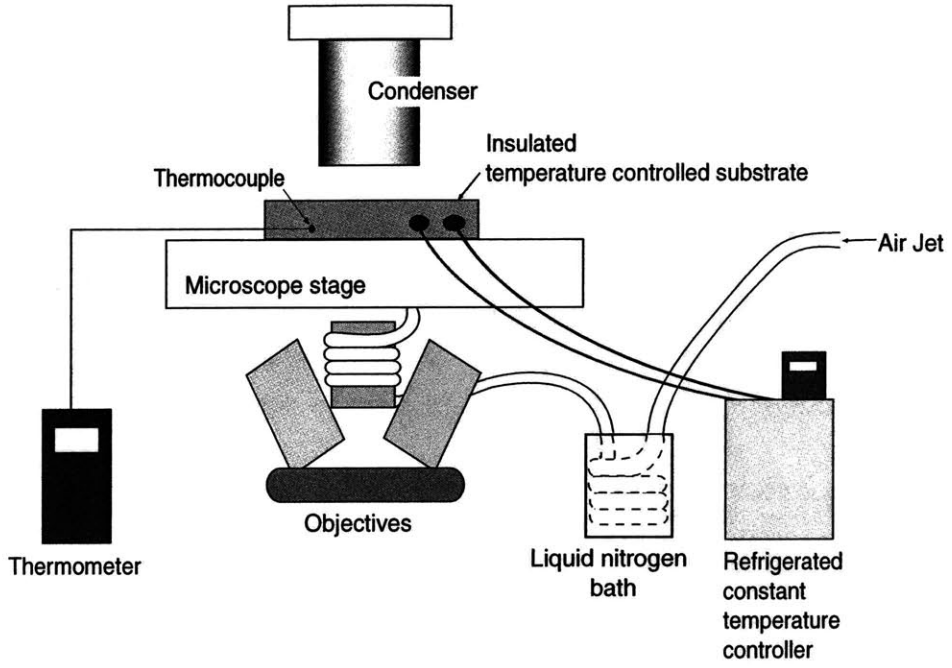

Figure 2-6: A schematic of experimental apparatus for temperature dependence measurement. When heating, only the refrigerated constant temperature controller is used. When cooling, a liquid Nitrogen is used to cool the air stream inside the tubing that wraps around the objective.

Measurement procedure

Experiments were carried about at four different temperatures, 9.7, 15.7, 24, or 32 °C. The protocol described in section 2.2.1 was used, with time in between various steps to ensure temperature equilibrium.

Data analysis

For the motion analysis of the recorded and digitized sequences, at least three representative reactions were analyzed at each of four different temperatures using the image analysis software GYROSCOPE. Each experiment was calibrated with an image of a stage micrometer.

2.2.2 Results

The magnitude of the velocity ranges from 1.7 μm/s at 9.6°C to 37μm/s at 32°C, and shows a systematic increase with temperature (Fig.2-7). The velocity varies

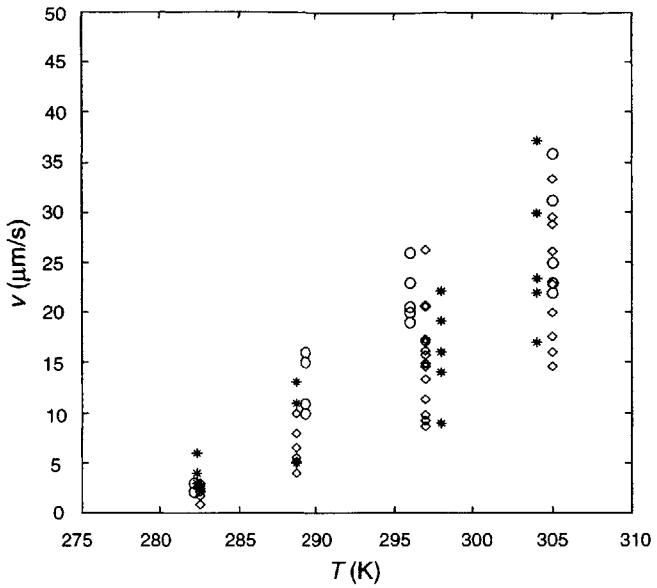

Figure 2-7: Velocity (v)-temperature (T) relationship in Limulus acrosomal process from three crabs at 4 different temperatures, 9.6, 15.7, 24, and 32°C. Each symbol represents a different crab and for each crab, at least three representative reactions were analyzed at each of four different temperatures. The velocity of the acrosomal process depends on the temperature, so that it increases as the temperature is raised. The velocity reaches a maximum value of about 37 μm/s at 32°C and minimum value of 1.7 μm/s at 9.6°C. The mean velocities among three crabs at each of four temperatures, 9.6, 15.7, 24, and 32 °C, are 2.9, 9.2, 16, and 24.9 μm/s with its standard deviation of 1.2, 3.9, 4.9, and 6.5 μm/s, respectively. These variations in velocity at each given temperature are due to possible viscous wall effect, concentration of calcium, and aging.

among different cells as much as 20% at a given temperature but there is a very clear inclination pattern of mean velocity as a function of temperature.

To relate the reaction rate with the temperature, we consider a case of kinetics in chemical reaction in which two components A and B combine into a compound AB. By applying the principles of statistical mechanics and chemical kinetics, we may write $R \sim e^{-E_a/k_BT}$, where R is the rate at which A and B produce AB, E_a is the activation energy, k_B is the Boltzmann's constant, T is the temperature is Kelvin, and e^{-E_a/k_BT} (Arrhenius factor), as a whole, represents the probability that the reaction will proceed [16]. In Fig. 2-8, A corresponds a latched scruin-actin complex and B calcium binding to calmodulin, AB an unlatched scruin-actin complex, and its reaction rate R the rate at which the scruin unlatches and the actin filaments untwist

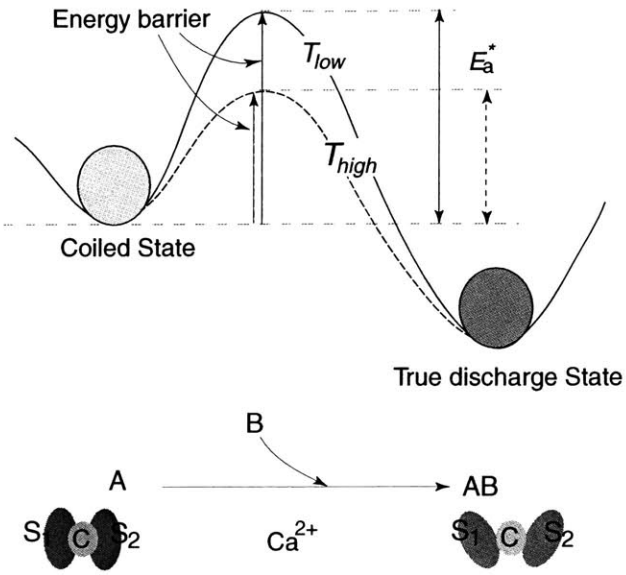

Figure 2-8: Energy diagram from the coiled state to the true discharge state. E_a^* represents the relative activation energy, $E_a^* = E_a/k_bT$. As temperature T is increased, the relative activation energy is decreased, resulting in a lower energy barrier between two states. With a lower energy barrier, it is more likely that the reaction will proceed from A to AB where A represents a latched scruin and AB refers to an unlatched scruin, and thus we expect an increase in its rate. S_1, S_2, and C refer to two domains of scruin and calmodulin, respectively.

with respect to one another. The positive correlation of the extension velocity with temperature is related with a decrease in the relative activation energy of the reaction. Consequently, the lower barrier between the coiled and uncoiled states enhances the reaction rate.

If the individual unlatching or untwisting events were independent and each event occurs randomly at a constant rate, the system would obey Poisson statistics. We would then expect the mean value of the velocity equals the variance of the velocity. As shown in Fig. 2-9, however, this is not the case here; the mean velocity and the variance of the velocity are not equal to each other. This indicates that the individual unlatching of scruin is not an independent but a cooperative process due to the elastic coupling between monomers in a filament [34].

So far, we have learned two facts about the unlatching event of the scruin molecules. One is that each unlatching event is localized and it propagates like a unzipping mech-

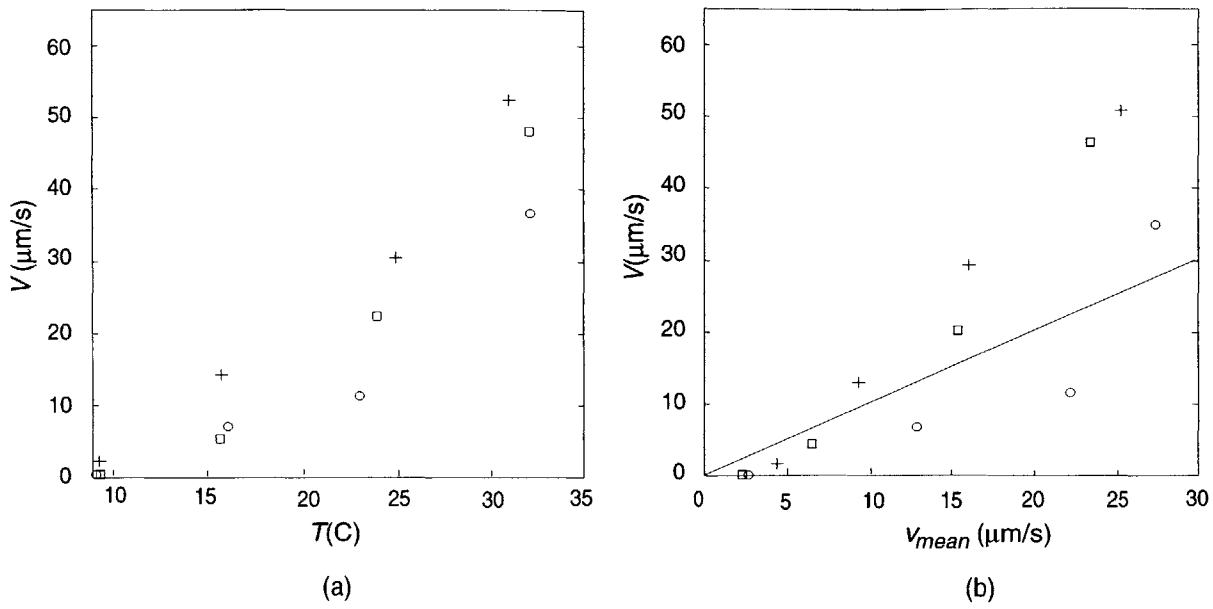

Figure 2-9: (a) Increase in variance (V) with increase in temperature (T): At four different temperatures (roughly 4, 16, 24 and 32°C), velocities of 5-10 sperms were measured and the variances at each temperature were computed based on the Eq 2.1. Each symbol represents a different batch of sperms on a different day. (b) Relationship between the variance (V) and the mean of the reaction velocity (v_{mean}): The linear graph represents the line at which the mean value equals the variance. If the scruin unlatching events were generated in accord with the Poisson process assumptions, the mean value and the variance would have been equal to each other.

anism. The other is that each of this unlatching event is cooperative rather than independent.

2.3 Morphological dependence on the acrosomal reaction velocity

At a given temperature, the average values of the acrosomal reaction rates differ from one batch to another besides the variation among individual cells. One batch of sperms means a pool of sperms collected from one crab at once. For example, the average acrosomal reaction rate of the sperms collected from one crab on March 3, 2000 was 7.1±1.1 μm/s, 12.9±2.9 μm/s on March 14, 2000, 9.0±1.3 μm/s on April 10, 2000, and 13.7±3.4 μm/s on May 15 while the temperature was somewhere between

21~24°C. To track down the causes of the variation in the data, we investigated whether there is any relationship between the reaction rate and the morphology of the sperms studied using electron microscope.

2.3.1 Experimental procedure

Six crabs were randomly picked and marked. Sperms were collected only once a week at the same time of the day. 1ml of sperms were collected from all 6 crabs and labeled clearly. Half of the collected sample was used for the velocity experiment and the other half was fixed and embedded for electron microscopy. The experiments were repeated three times.

Velocity measurement using light microscopy

Velocity measurement experiments were carried out as described in section 2.1.1. Each step of the experiment was carefully scheduled and repeated in the same way for each trial (See Table 2.1). For each batch of sperms, the acrosomal reactions were induced by adding the calcium ionophore A23187, and 5-10 different reactions were recorded at a controlled temperature (26±0.6°C). Each recorded movie was digitized, and the velocity of each reaction was measured by fitting the elongation distance vs. time plot to the first order linear graph. Then, the average value of the 5-10 velocities was calculated for each batch. The batches with the slowest and the fastest average velocity were selected for further electron micrograph analysis.

Electron microscopy

The sample preparation for the electron microscopy was kindly performed by Nicki Watson from the Whitehead Institute, Cambridge, MA [37]. Six batches of sperm were washed once in ASW (Artificial Sea Water) and then fixed in 2% glutaraldehyde in ASW one batch at a time at the same time as the velocity measurement experiment. Timing of this fixing step was done with care to minimize any discrepancy between two procedures, namely the velocity measurement experiment and the electron microscopy experiment. After fixing for an hour, the sperms were washed briefly in ASW and

Table 2.1: Schedule for Morphology experiment.

Time	Step
10:30 am	Collect sperms from each of 5 selected crabs
12:00 pm	Wash sperms by short spin in ASW
12:20 pm	Dilute sperms of crab 1 in 25mM $CaCl_2$ in ASW, 1:1000
12:30 pm	Prepare a freshly diluted calcium ionophore
12:40 pm	Begin the experiment and fix sperms from crab 1 in 2% glutaraldehyde in ASW
1:30 pm	Dilute sperms of crab 2 in 25mM $CaCl_2$ in ASW, 1:1000
1:40 pm	Prepare a freshly diluted calcium ionophore
1:50 pm	Begin the experiment with sperms from crab 2 and fix them for EM simultaneously
3:00 pm	Dilute sperms of crab 3 in 25mM $CaCl_2$ in ASW, 1:1000
3:10 pm	Prepare a freshly diluted calcium ionophore
3:20 pm	Begin the experiment with sperms from crab 3 and fix them for EM simultaneously
4:00 pm	Dilute sperms of crab 4 in 25mM $CaCl_2$ in ASW, 1:1000
4:10 pm	Prepare a freshly diluted calcium ionophore
4:20 pm	Begin the experiment with sperms from crab 4 and fix them for EM simultaneously
5:00 pm	Dilute sperms of crab 5 in 25mM $CaCl_2$ in ASW, 1:1000
5:10 pm	Prepare a freshly diluted calcium ionophore
5:20 pm	Begin the experiment with sperms from crab 5 and fix them for EM simultaneously
6:00 pm	Dilute sperms of crab 6 in 25mM $CaCl_2$ in ASW, 1:1000
6:10 pm	Prepare a freshly diluted calcium ionophore
6:20 pm	Begin the experiment with sperms from crab 6 and fix them for EM simultaneously

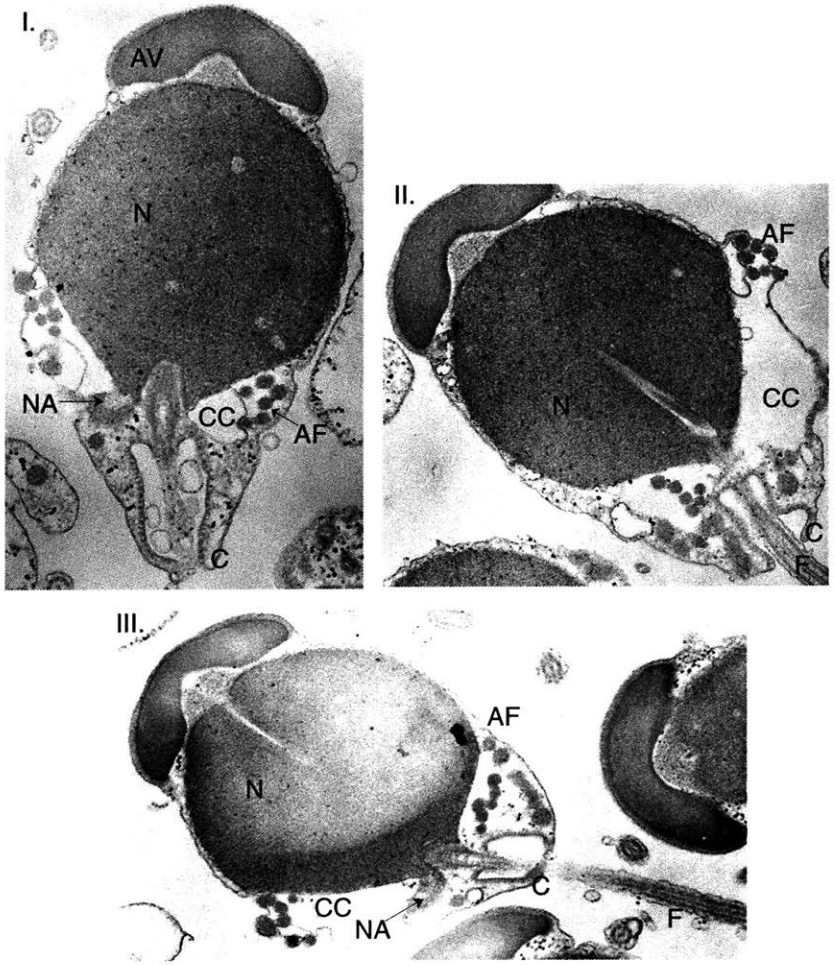

Figure 2-10: Selected *Limulus* spermatozoon from morphology experiment. I. II. and III. indicate a batch from crab no. 5, 1, and 4, respectively. I and III were the slowest while II was the fastest batch. As evident from these images, all of them show indistinguishable morphological features: AV. Acrosomal Vesicle, AF. Acrosomal filament, N. Nucleus, NA. Nuclear appendage, CC. Circumnuclear cisternae, C. Collar, F. flagellum

fixed in 1% O_sO_4 in 0.1 M phosphate buffer at pH 7 for 1 hour at 0°C. The sperm were then dehydrated in acetone and embedded in Araldite.

The fastest and the slowest batches were selected from the previously described velocity measurement procedure and thin sections of those two fixed and embedded samples were cut with a diamond knife on a Sorvall Porter-Blum Ultramicrotome II. The cut sections were stained with uranyl acetate and lead citrate, and viewed in a Philips 200 electron microscope.

Electron micrographs of the sections from two extreme batches at different magnifications were compared to see if there is any morphological difference between two

extremes. Also, sperms from each batch were compared. The same procedure was repeated three times.

2.3.2 Size measurement

Fahrenbach mentioned in his paper that immature sperms tend to have shorter acrosomal process ($\sim$ 25μm) while the mature length of the acrosome bundle reaches about 50μm [14]. To find out whether there is any correlation between the size of the sperm and the reaction rate, sizes of 20-30 randomly picked sperms were measured and compared with their reaction velocity. Four values were measured from the digitized images of the acrosomal reactions from three batches. Although there involved some degree of inaccuracy in measuring the size of the three dimensional sperm head from digitized one dimensional images, special care was taken to keep consistency in measurement. For example, measurements were taken only on those sperms that are lying perfectly in the plane of focus from the top to the bottom so that the acrosomal vesicle appears clearly as about 1/5 of the sperm head. The measurements from each experiment were calibrated with the digitized images of a stage micrometer.

2.3.3 Results

Morphological dependence

Fahrenbach reported morphology of spermatozoon at different developmental stages [14]. In his studies, testes of mature male were fixed and sectioned at various times of the year. Consequently, he could observe different features of developing spermatozoa before they filled the seminifereous tubules to be ejaculated upon stimulation. Fahrenbach describes that as the meiosis progresses spermatids join to one another by intercellular bridges in group of four. Once the bridges are disintegrated, most aspects of the spermatozoa are completely differentiated. At a late stage in spermiogenesis, the yet-immature spermatozoa fill the seminiferous tubules where they mature further to be released. Yet, occasionally immature spermatozoa are also released by early rupture of cysts.

The easiest way to distinguish mature sperms from the immature ones may be the

nuclear appendage (See Fig.2-10) since the nuclear appendage develops most slowly. It starts as a crescentric region of uncondensed chromatin next to the nuclear envelop and comes to completion (0.4-0.6 μm) last in the mature spermatozoon. The collar (C in Fig.2-10) is another feature that can be relatively easily distinguished in mature spermatozoa. In mature sperms, the length of the collar reaches $\sim 1.7\mu$m, and the collar wall becomes unsymmetrical. The number of loops in the coil may also be used to determine the maturity of the sperm since the filaments grow as it develops. Lastly, the widely dilated circumnuclear cisternae withe the contained acrosomal bundle are characteristic of a mature spermatozoon.

We were able to find all of the four distinct features that differentiate mature sperms from the immature ones. Based on what we observed, however, we could not find any morphological differences between the slowest and the fastest batches of the sperms. All of them had 1) well developed collars, although their lengths and thickness varied, 2) at least 6 loops in the coil, and 3) widely dilated circumnuclear cisternae at the posterior end of the nucleus (see Fig.2-10). These observations imply that the sperms used for our experiments were all in fact matured ones, and thus they exhibit more or less identical morphology. Fahrenbach said in his report that fully mature spermatozoa are observed mostly during the breeding season, which is late spring. Our morphological dependence experiment was done in June. If what Fahrenbach observed is correct, it may be no surprise to observe no obvious morphological differences. Unless we collect sperms directly from testes before and after they mature, and repeat the same experiment, it seems to be difficult to correlate the reaction rate to morphology of the spermatozoa.

We also looked if the slowest or the fastest batch of sperms was consistently the slowest or the fastest for this may indicate that the particular crab is unusually unhealthier than normal or exceptionally healthier than the rest. However, as indicated in table 2.2, there was no consistency in which of the batches was the slowest or the fastest. For instance, the batch from crab 4 was the slowest on the first two trials and the fastest on the last trial. The average reaction rate of the batch from crab 1 was once $31.1\pm4.4\mu$m/s while it was only $15.9\pm10.6\mu$m/s in other time, which suggests

Table 2.2: Chart for the average velocity of sperms from 6 selected crabs for three trials (velocities in μm/s): '$\pm$' indicates the standard deviation.

Trial no. V_{ave}	crab 1	crab 2	crab 3	crab 4	crab 5	crab 6
I. V_{ave}	31.1$\pm$4.4 fastest	23.6$\pm$8.7	24.9$\pm$5.0	15.8$\pm$6.2 slowest	15.3$\pm$6.2 slowest	26.8$\pm$10.9
II. V_{ave}	19.4$\pm$5.4	26.8$\pm$14.9 fastest	21.0$\pm$4.3	18.5$\pm$6.5	14.8$\pm$3.5 slowest	16.3$\pm$5.4
III. V_{ave}	15.9$\pm$10.6	13.3$\pm$1.8	13.1$\pm$3.5	17.6$\pm$7.6 fastest	17.6$\pm$5.1 fastest	11.1$\pm$2.1 slowest

Table 2.3: Average size comparison among three batches (in μm) : '$\pm$' indicates the standard deviation in the data.

Batch no.	$V_{ave}(\mu m/s)$	length	width	flagella	acrosome
I	7.1$\pm$1.1	6.5$\pm$0.5	5.1$\pm$0.3	35.3$\pm$2.2	59.4$\pm$2.8
II	9.0$\pm$1.3	6.4$\pm$0.4	5.1$\pm$0.6	37.4$\pm$3.0	61.5$\pm$4.5
III	12.9$\pm$2.9	6.2$\pm$0.4	4.9$\pm$0.3	35.8$\pm$2.7	62.8$\pm$4.6

that it be random.

Size dependence

The results from the size dependence experiment are summarized in table 2.3. As one can notice, there is no obvious trend between the sizes and the average reaction rate. Although there seems to be a slight increase in the length of the acrosomal process with the increase in the average reaction rate, these results are not conclusive since the differences in their average values are smaller than the variations in the data.

2.4 Effect of viscosity on acrosomal reaction velocity

The velocity of an object moving in a low Re environment depends on the net force applied. In order to study the effects of the environment and determine if viscous resistance is what limits the speed of the acrosomal reaction, the viscosity of the medium through which the acrosomal process extends was raised to several different values.

By investigating the influence of viscosity on the velocity of the extension reaction, it is possible to learn the relative significance of resisting mechanisms present in the system.

2.4.1 Selection of viscous medium

In the context of experiment, the viscous solution for our experiment must be chemically inert so that it does not interfere with the acrosomal reaction both chemically and mechanically. Its pH, ionic strength, and its composition should remain as close to the sea water as possible. Hunt et al. [21] have tried four different solutions in searching an appropriate viscous medium for the microtubule motility assays and eventually used a composite liquid called visc-mix, made of a combination of long chain polymers and spherical polymers which seemed to best.

Since the diameter of microtubules is about 30 nm, comparable to that of the acrosomal process,the polymers used for the visc-mix should also work for our purpose. A modified visc-mix, called visc-mix II, was prepared and used in our experiments.

Preparation of the medium

Visc-mix II-1 100% stock solution consists of 10%(w/v) dextran (Sigma, average molecule mass 67kDa) and 5% Ficoll-400 (Sigma, molecule mass 400kDa) in 25mM $CaCl_2$ artificial sea water (ASW). These stock solutions were diluted further into 5 different concentration with 25mM $CaCl_2$ ASW to obtain a series of viscous solutions. 100% stock solution, 80%, 50%, 30%, and 10% dilutions were made, and well-mixed

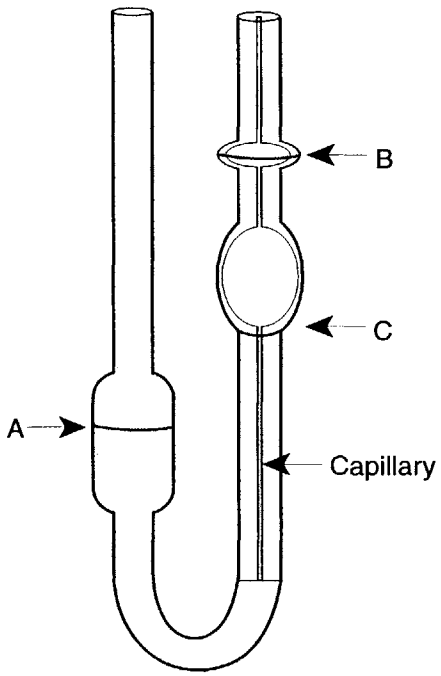

Figure 2-11: A schematic of a U-shape ubbelohde viscometer.

with a magnetic stirrer. Visc-mix II-2 100% stock was made of 8%(w/v) dextran and 4% Ficoll-400, and it was diluted further into 70, 50, and 20%. Visc-mix II-3 100% stock consists of 7.5%(w/v) dextran and 3.75% Ficoll-400, and a 60% and a 45% dilutions were made. All solutions were kept at 4°C to prevent any bacterial growth.

Viscosity measurement

For series of diluted visc-mix II solutions used in our experiment, three different U-shape Ubbelohde viscometers (Technical Glass Products, Inc) were utilized (see Fig. 2-11). Each solution was loaded into an appropriate viscometer upto the line indicated as A, and the solution inside the tube was drawn with suction until the upper meniscus reaches about 1cm above the line indicated as B. As the liquid passed through the line B, we began timing until the upper meniscus reached the line C.

These U-shape Ubbelohde viscometers measure kinematic viscosity. Therefore, the densities of each diluted solution of visc-mix II were also needed to be known. To minimize any errors, the solution was very slowly pipetted in, the pipette tip

Table 2.4: Viscometers used to measure the kinematic viscosity of the visc-mix II-1, 2, 3: CC indicates a calibration constant provided for each viscometer at a given temperature.

No.	Range(cs)	CC at $20°C(cs/s)$	Visc-mix
1	20-100	0.10655	II-1 (100, 80%), II-2 (100%), II-3 (100%)
2	3-20	0.01497	II-1 (50, 30%), II-2 (70%),II-3 (65%)
3	0.3-3	0.0112	II-1 (10%), II-2 (50, 10%),II-3 (45%)

was left in the solution for a sufficient time, and the mass of both pipette tip and the liquid inside the tip was measured using a scale (Mettler-Toledo, Inc (Model: AB104)). The scale was set to zero with a clean pipette tip on it. Measurements were repeated 3 times for each dilution. For each dilution, pipetted volume and its mass were recorded, and the dynamic viscosity (DV) was obtained by multiplying the kinematic viscosity (KV) and the corresponding density of the medium (See table 2.5).

2.4.2 Apparatus setup and sample preparation

The capillary flow cell was situated in a temperature-controlled stage described in section 2.2.1 whose temperature is regulated by circulation of cooled water. Temperature of the refrigerated constant temperature circulator was set at 10°C and the temperature of the sample was measured to be 25.1±0.4°C.

Preparing sperm sample

We followed the same procedure as in 2.1.1. The washed and resuspended sperm sample was then divided equally into 6 tubes. Sperms in number 1 tube was diluted with artificial sea water (ASW) with 25 mM $CaCl_2$, 1:200. Ones in number 2, 3, 4 and 5 were diluted 1:200 with the prepared 10%, 30%, 50%, 80%, and 100% visc-mix II, respectively. Calcium ionophore A23187 (2mg/ml in 95% ethanol) was diluted in the ASW, 1:100. For previous experiments in section 2.1 and 2.2, A23187 dissolved in DMSO was used. Since DMSO is toxic, we began to use 95% ethanol instead.

Table 2.5: Viscosity of each dilution measured with U-shape Ubbelohde Viscometer: (1) Composition(%in w/v): D indicates dextran(67kDa) and F indicates Ficoll-400 (400kDa), (2) Concentration, (3) Kinematic Viscosity (cs), (4) Density(kg/m^3), (5) Dynamic Viscosity (cp).

Visc-mix	Composition	Concentration(%)	KV(cs)	Density(kg/m^3)	DV(cp)
II-1	10%D-5%F	100	36.44	1080	33.7
		80	20.54	1073	19.1
		50	7.78	1059	7.34
		30	4.4	041	4.23
		10	1.53	1014	1.51
II-2	8%D-4%F	100	29.13	1072	27.2
		70	12.16	1050	11.58
		50	5.69	1038	5.47
		30	2.81	1025	2.74
II-3	7.5%D-3.75%F	100	28.77	1065	27.0
		65	7.33	1051	6.98
		45	4.86	1038	4.68

A23187 can be dissolved better in completely in ethanol at low concentration. Above 2mg/ml, however, it is necessary to increase the temperature of solvent to ~45%°C and wait till the A23187 powder is completely dissolved. Sonication of the solution often helps as well. Once it is completely dissolved, the stock should be aliquoted and kept in a freezer for later use. It is recommended that all the dilutions be made fresh right before the experiment and all the samples be kept on ice unless otherwise specified.

Recording, digitization, and measurement

Each diluted sperm sample in different solutions was pipetted into the flow cell and 10μl of diluted ionophore was added to induce the reaction. The images were acquired with a Dage MTI camera and recorded with a Sony SVO-9500MD Super-VHS video recorder. Images were then digitized using a SNAPPER frame grabber and a OPEN-

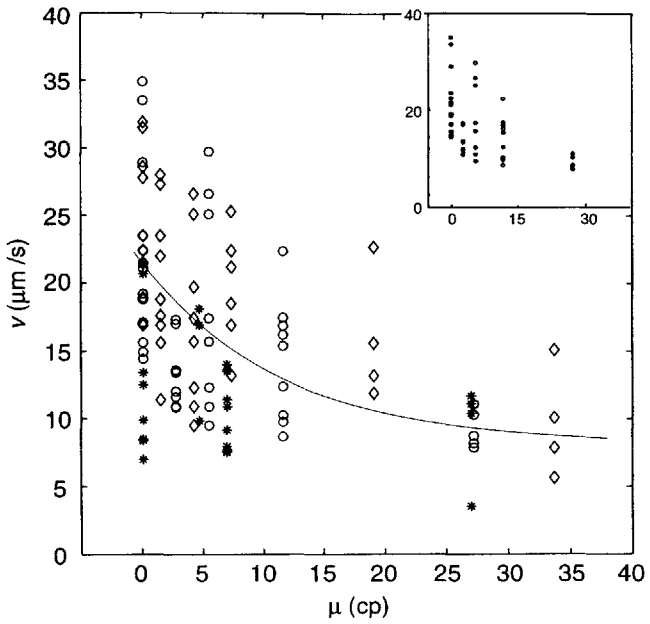

Figure 2-12: A plot of the reaction velocity (v) as a function of viscosity (μ) of the medium (in cp: 1cp=10^{-3}kg/m·s). Each symbol ($\diamond$, $\circ$, and $*$) represents a set of experiment done with visc-mix II-1, II-2, and II-3, respectively. Although there is a great deal of variation in the data at each viscosity, we observe a negative correlation between the reaction rate and the viscosity. The inset is the data from Visc-mix II-2 only, which exhibits a clearer correlation. The axes are the same as the main plot. The solid line is the curve that best fits the experimental data: v=$exp(-0.085 \cdot \mu + 2.8) + 8.1$.

LAB software (Improvision, Inc). All the velocity measurements were made using OPENLAB. As in section 2.1.1, an incremental extension distance was measured for each frame and the data were saved as a mat file. The elongation was then plotted as a function of time using MATLAB.

2.4.3 Results and discussions

As shown in the Fig. 2-12, there is an overall negative correlation between the reaction rate and the viscosity of the medium. In the region from 1cp to 10cp, it appears that the variations present among measurements at each viscosity are so large that no conclusive trend is observed although the trend is more clear in each set of experiment (See inset of Fig. 2-12). Provided the same amount of initial energy, the rate of the acrosomal reaction in a highly viscous medium is expected to become slower owing to

higher viscous dissipation acting against the moving acrosome. Below 10cp, however, the increase in viscosity does not seem to affect the reaction rate as much as one may expect. This may suggest that the energy supply in the system is sufficient to overcome the extra drag exerted by the medium upto a certain limit. The effect of the external load becomes apparent as the viscosity of the medium exceeds 25cp, which is 25 times greater than that of water. The average velocities measured in ASW (1cp) and in the 100% visc-mix differ by more than 2 folds.

Variations in the data within each experiment may be due to the proximity of the extending acrosome to the coverslips, a spatially inhomogeneous distribution of Ca^{2+} or ionophore, the inhomogeneity in fluid viscosity, and the individual difference among sperm cells (discussed in Section 2.1.2). Variations in the average velocity among three experiments may be due to the individual difference in crab's health or condition.

We could not increase the viscosity of the medium any further for the following experimental difficulties. When a solution of 57.8cs was used, we first had a difficult time adding sperm cells into the solution. Sperm cells were all aggregated and made it difficult to monitor a reaction happening. Moreover, having a highly viscous solution inside flow cell resulted in poor optics.

When we measured the viscosities of the prepared solutions, we only measured macroscopic viscosities without considering what the microscopic behavior of the polymer solution could be. Therefore, there remains one concern about the microscopic viscosity measurement. As mentioned earlier, it is crucial to have polymers whose sizes are smaller than the diameter of the acrosomal bundle to avoid the problem of having a behavior like porous gel. Hunt et al measured a microscopic viscosity of their vics-mix by analyzing the Brownian motion of fluorescent latex beads and microtubules in it. From this study, they found that the Brownian motion was in good agreement with the macroscopic viscosity, and there was no indication of porous gel-like behavior. The diameter of Ficoll-400 is 3.5nm, and the diameter of dextran is estimated to be about 6nm. The solute molecules are about 5-10 fold smaller than the diameter of the microtubules. Since the diameter of the acrosomal bundle is approxi-

mately 3 times that of microtubule, it seems reasonable to assume that the polymers used are sufficiently small compared to the diameter of the acrosomal bundle, and thus it is unlikely that our solutions, visc-mix II series, would behave like a porous gel.

Chapter 3

Estimation of energy involved during the reaction

3.1 Introduction

Mahadevan has previously performed a first order approximation of the energy involved in the acrosomal process based on results from Tilney and DeRosier [8, 9, 10, 52]. This chapter is based on the discussion of the energy estimation from our preprint [34].

As mentioned in chapter 1, we learned that there is no ATP or actin polymerization involved in the acrosomal reaction but only two proteins, actin and scruin, that undergo a dramatic conformational change in the presence of Ca^{2+}. From the biochemical and structural studies on the actin and scruin along with calmodulin, it has been hypothesized that the energy arises as the initially bent and twisted actin bundle straightens out, most of which is dissipated hydrodynamically during the process. Based on this hypothesis, we now estimate the total energy involved in the reaction.

3.2 Strain energy stored in the coil

In this section, the initially stored mechanical potential energy in the coil is estimated. Observation of true discharge reaction using a light microscope with a $100\times$ objective reveals no fluctuations in its shape, which allows us to treat the bundle as an overdamped elastic rod. Electron micrographs of the acrosomal bundle shows that

the bundle is tapered from 85 actin filaments on its posterior end to 15 filaments on its anterior end (lying in the nuclear channel). For simplicity of the analysis, however, we assume a uniform cross-sectional area along the bundle for now. Also, considering that the filaments are hexagonally packed in the bundle, we may assume that the rod is isotropic to a first approximation, i.e., the elastic properties are the same in all directions.

In its coiled state, the bundle is a twisted and bent rod latched by scruin molecules. DeRosier and Tilney [10] estimated from electron micrographs of the freeze-fracture pictures and diffraction patterns that the filaments in the bundle are over-twisted by 0.23° per monomer. In addition, as shown in Fig.1-3, the bundle is not uniformly bent into a smooth loop but kinked into a polygonal shape with 14 elbow and arms. Mahadevan et al.[34] proposed that these kinks be low-angle tilt boundaries [36] induced by the differential sliding between the actin filaments.

The stored energy in a twisted and bent isotropic circular rod, which is naturally straight, is

$$U = \frac{1}{2}\int (EI\kappa^2 + GI_p\tau^2)dx$$

which can be simplified for constant EI, GI_p, κ and τ as

$$U = \frac{L}{2}(EI\kappa^2 + GI_p\tau^2) \tag{3.1}$$

where EI is the bending stiffness of the actin bundle, GI_p is the twisting stiffness, κ is the curvature of the coil, τ is the twist per unit length, and L is the total length of the bundle [30]. The bending stiffness (flexural rigidity), EI, is a product of Young's modulus E and the moment of inertia I, and it is the measure of the resistance of a rod to bending. The twisting stiffness (torsional rigidity), GI_p, is an analogous form of EI for twisting, and represented as a product of the shear modulus G and the polar moment of inertia I_p. The $EI\kappa^2$ term represents the energy associated with bending while $GI_p\tau^2$ represents the twisting energy of the actin filaments.

The energy associated with the edge dislocation in the kinks scales as the angle between two polygonal sides, and is typically much smaller than that in the uniformly distributed twist deformation [34]. Therefore, we assume that energy released

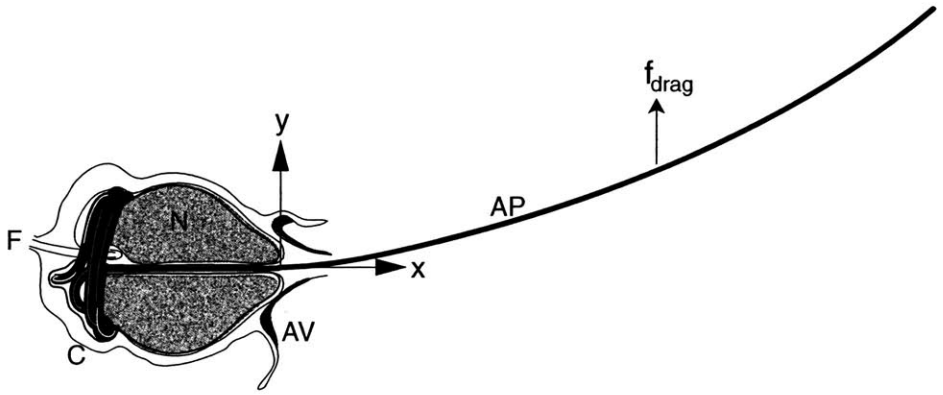

Figure 3-1: External drag force (f_{drag}) must balance the internal elastic bending force as the acrosomal process extends out through medium which can be modeled as an elastic rod moving through a viscous liquid. N: nucleus, C: coiled bundle, AV: ruptured acrosomal vesicle, AP: acrosomal process, F: flagellum.

from untwisting of the actin filaments dominates over the energy released from the unbending events of the kinks by differential sliding, which permits us to write

$$U \sim \frac{L}{2} G I_p \tau^2. \tag{3.2}$$

Since there is $\sim 840°$ twist per loop of coil whose circumference is approximately 10μm [8], we obtain a twisting strain per unit length, $\tau \sim 84°/\mu m = 1.5 rad/\mu m$.

To estimate the mechanical properties of the acrosomal process, we consider the dynamics of an elastic rod bending in a viscous medium (See Fig. 3-1). As the rod moves in the viscous liquid, the elastic bending force must be balanced by the hydrodynamic drag force exerted against its bending motion, and this relation can be written as

$$\zeta \frac{\partial y(x,t)}{\partial t} = EI \frac{\partial^4 y}{\partial x^4} \tag{3.3}$$

where ζ is a drag coefficient per unit length for transverse motion (See chapter 4.2 for derivation). By scaling analysis, we have

$$l \approx (EI/\zeta\omega)^{1/4} \tag{3.4}$$

where l is the characteristic length in x, and ω is the characteristic time. Careful observation of the decay of bending disturbances in the bundle reveals that the bundle oscillations are dominated by the dynamics of the lowest mode with $\lambda = 2l$. The

lowest mode is the slowest mode which approximates the shape of the acrosomal bundle during the relaxation (See Appendix A and Fig. A.6.). ζ for a long circular rod moving in an unbounded medium is solved by Tirado and Garcia de la Torre (1979), and is given in Table 4.1 as

$$\zeta = \frac{4\pi\mu}{[ln(l/2r) + 0.84]} \sim 2 \times 10^{-3} kg/m \cdot s$$

where μ is the viscosity of water,$\sim 10^{-3}$ kg/ms, l the length of the bundle, 60μm, and r the average radius of the bundle, 35nm. Using ζ, l and $\omega \sim 0.5s^{-1}$, we find EI from the Eq.2.3 to be $\sim 2.6 \times 10^{-12}$ dynes$\cdot$ cm^2 (2.6×10^{-20} Nm^2). Since $EI \sim GI_p$ for an isotropic circular rod, the stored energy in the coil can be estimated using the Eq.(3.1) with given parameter values as

$$U \sim \frac{L}{2} GI_p \tau^2 \approx 1.75 \times 10^{-5} ergs (1.75 \times 10^{-12} J)$$

.

3.3 Hydrodynamic energy dissipated during the extension

Here, we consider a case in cellular biological scale, with its typical length L in micrometers , time t in seconds, and a kinematic viscosity ν to be about that of water ($\sim 10^{-6}$ m^2/s). Based on the average diameter of the acrosomal bundle ($\sim$ 50nm) and the velocity of the acrosomal reaction ($\sim 15\mu$ m/s), the Reynolds number is, Re= $UD/\nu \approx 10^{-14}/10^{-6} \approx 10^{-8}$. This represents a low-Reynolds number or Stokesian regime in which a viscous effect dominates over an inertial effect.

Based on the unzipping mechanism for extension, the reaction proceeds as the scruin and actin change their conformation subunit by subunit. The potential energy is then converted to translational work which is then dissipated during the passage of the bundle through the nuclear channel and the viscous environment of the sperm. What are other sources of dissipation during the reaction? There are viscous dissipation occurring outside the sperm, rotational drag in addition to the translational

drag, end effects of the entrance and exit of the nuclear channel, sliding friction between filaments, and work to stretch membrane as the acrosomal process carries the outer membrane of the sperm during extension.

The nuclear channel is very narrow, and the clearance between the channel wall and the bundle surface is only of the order of a few nm (while the average diameter of the bundle is approximately 70nm). Therefore, we may assume that the dissipated energy by translational drag inside the nuclear channel dominates over that in the free medium outside the sperm head. As pointed out in chapter 1, the bundle not only extends forward but also rotates around its axis due to its relaxation of the helical structural feature from the coiled state. This effect due to rotational drag is also assumed to be negligible compared to the translational drag inside the nuclear channel since the diameter of the bundle is about three orders of magnitude smaller than the length of the bundle. To simplify the analysis further, we may ignore the small end effects associated with the entry and the exit of the bundle into and out of the nuclear channel. Also, it is likely that there would be some energy loss due to frictional sliding between actin filaments during the uncoiling, but this effect should be small and thus neglected in this analysis.

It has been observed from electron micrographs of the acrosomal process that the extending acrosomal bundle is surrounded by a outer plasma membrane of the sperm head. Is the membrane being stretched 60μm from its unstretched form during the reaction? Carefully studying the electron micrographs of the thin sectioned sperm head, one may notice that the plasma membrane around the sperm head is severely wrinkled. This observation is consistent with the fact that a polymer, an analogue of a membrane, exists as a highly disordered wrinkled form in its stress-free equilibrium state. Presence of wrinkles in the *Limulus* membrane suggests a plausible mechanism of *unfolding* of the wrinkles rather than *stretching* during the extension of 60μm acrosomal bundle, and the associated energy with unfolding is assumed to be small compared to hydrodynamic dissipation energy. Based on these assumptions, we assume that most of the stored energy is dissipated hydrodynamically inside the nuclear channel, which will provide us a lower bound of the required energy in the

system. Validity of the stated assumptions will be discussed in the following section, chapter 3.4.

The total rate of energy dissipation due to viscosity is

$$\frac{dE}{dt} = \dot{E} = \iiint_V \mu(\nabla \mathbf{u})^2 dV.$$

In a cylindrical coordinate, this is simply

$$\dot{E} = \iiint_V \mu(\nabla \mathbf{u})^2 r dr d\theta dz. \tag{3.5}$$

As shown in this equation, we must know the velocity profile $\mathbf{u}$ of the fluid inside the nuclear channel in order to obtain the energy rate $\dot{E}$. The acrosome bundle moving through a nuclear channel can be modeled as a cylindrical rod moving axially inside a stationary circular cylinder (See Fig.3-2). For the case of viscous liquid flowing through a long straight tube of circular cross-section, the streamlines of the flow should be all parallel to the cylinder axis. Therefore, the radial and tangential velocity components are zero (u_r=u_θ=0). Due to the axial symmetry of the flow, the axial velocity component u_z is only the function of the radial coordinate r. For an incompressible fluid with constant viscosity μ and no gravitation effect, the governing equation (the Navier–Stokes equation) takes the form of

$$\frac{D\mathbf{u}}{Dt} = \frac{-1}{\rho}\nabla p + \nu \nabla^2 \mathbf{u}. \tag{3.6}$$

For the circular Poiseuille flow in the nuclear channel, the Navier–Stokes equation can be simplified to the form:

$$\frac{1}{r}\frac{d}{dr}(r\frac{du_z}{dr}) = \frac{1}{\mu}\frac{dp}{dz}. \tag{3.7}$$

The general solution of this equation is

$$u_z = \frac{1}{4\mu}\frac{dp}{dz}r^2 + C_1 \ln r + C_2. \tag{3.8}$$

Although p is a function of the axial coordinate z, the pressure gradient dp/dz is constant, which permits us to set

$$C_3 = \frac{1}{4\mu}\frac{dp}{dz}. \tag{3.9}$$

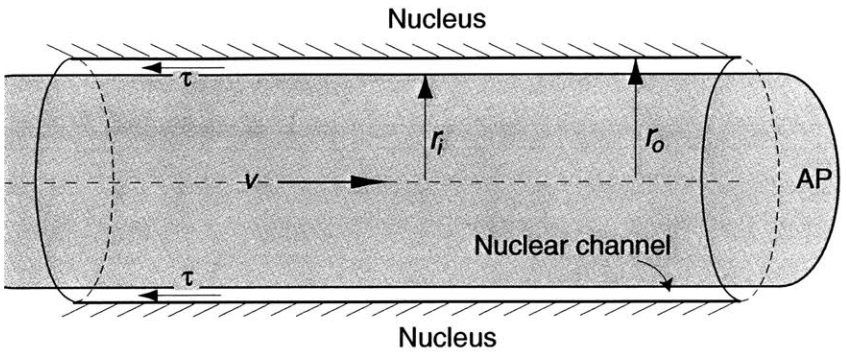

Figure 3-2: A schematic of the acrosomal bundle moving through a nuclear channel. AP stands for the acrosomal process, τ is the shear drag along the bundle, r_i is the average radius of the bundle, 0.035μm, and r_o is the radius of the channel, 0.040μm.

Now we need three boundary conditions for three unknowns C_1, C_2, and C_3. The appropriate boundary conditions are

$$u_z = -v \quad \text{at} \quad r = r_i \tag{3.10}$$

$$u_z = 0 \quad \text{at} \quad r = r_o \tag{3.11}$$

$$Q = 2\pi \int_{r_i}^{r_o} u_z r dr = \langle u_z \rangle 2\pi r_o (r_o - r_i) \tag{3.12}$$

where r_i is the radius of the inner cylinder (the acrosome bundle), r_o is the radius of the outer cylinder (the nuclear channel), v is the velocity of the acrosome bundle, and Q is the net flow through the annulus which is $\langle u_z \rangle 2\pi r_o (r_o - r_i)$ in this case (See Fig.3-2) where $\langle u_z \rangle$ the average velocity of fluid (v/2).

By substituting Eq. 3.10 and 3.11, we get

$$u_z = C_3 \left[{r_o}^2 - r^2 + \frac{\ln(r/r_o)({r_o}^2 - {r_i}^2)}{\ln(r_o/r_i)} \right] + v \frac{\ln(r_o/r)}{\ln(r_o/r_i)}. \tag{3.13}$$

Eq. 3.13 can be plugged into Eq. 3.12 to obtain the expression for C_3 using a software Maple (Waterloo Maple Inc):

$$C_3 = \frac{-3v\left[2(r_i - r_o) + r_o \ln(r_i/r_o)(r_i - r_o - 2)\right]}{2\left[(2{r_i}^3 - 3{r_o}^3 + {r_o}^3)\ln(r_i/r_o) - 3({r_o}^3 - {r_i}^2 r_o - {r_o}^2 r_i + {r_i}^3)\right]}$$

By replacing the C_3 in Eq. 3.11, we obtain u_z:

$$u_z = \frac{-3v\left[2(r_i - r_o) + r_o \ln(\frac{r_i}{r_o})(r_i - r_o - 2)\right]\left[{r_o}^2 - r^2 + \frac{\ln(r/r_o)({r_o}^2 - {r_i}^2)}{\ln(r_o/r_i)}\right]}{2\left[(2{r_i}^3 - 3{r_o}^3 + {r_o}^3)\ln(r_i/r_o) - 3({r_o}^3 - {r_i}^2 r_o - {r_o}^2 r_i + {r_i}^3)\right]} + \frac{v\ln(\frac{r_o}{r})}{\ln(\frac{r_o}{r_i})}. \tag{3.14}$$

Given this velocity profile, we now go back to Eq. 3.5 to solve for $\dot{E}$. As mentioned, there is only axial velocity component u_z in this problem, and u_z depends only on the radial coordinate r. Therefore, $\nabla \mathbf{u} = du_z/dr$. We first differentiate u_z (Eq. 3.14) with respect to r, and the result is squared to be integrated over the entire volume of $0 \leq z \leq l$, $0 \leq \theta \leq 2\pi$, and $r_i \leq r \leq r_o$. From calibrated electron micrographs of the thin sectioned *Limulus* sperm [37], r_o, r_i, and l (length of the channel) are measured, and their values are $r_i \approx 0.035\mu$m, $r_o \approx 0.040\mu$m, and $l \approx 5\mu$m. μ of the cytoplasm was assumed to be that of water to a first approximation, and a typical extension velocity is $v \approx 15\mu$m/s. Given these values, we obtain

$$\dot{E} = 2.2 \times 10^{-16} J/s = 2.2 \times 10^{-9} ergs/s$$

Since the velocity is constant and the average duration of the reaction is typically about $5s$, an estimate of the total energy dissipated during the reaction is of the order of $\dot{E}t \approx 1.1 \times 10^{-8} ergs$. We must remember, however, that the velocity of the acrosomal reaction varies from 1.7 μm/s to 37 μm/s depending on temperature. With the slowest velocity, the dissipated energy is approximately $1.4\times\ 10^{-10}$ ergs while the highest value of the velocity yields the dissipated energy inside the nuclear channel to be $\sim 6.7\times\ 10^{-8}$ergs, which is still one order of magnitude smaller than the estimated energy stored in the coil. Thus, the hydrodynamic dissipation in the nuclear channel provides us the lower bound estimate of the energy stored in the coil.

3.3.1 Validity of assumptions in estimation

To verify the validity of our assumptions, we can first compare energy dissipated inside and outside the nuclear channel due to translational drag in the fluid. Then the energy dissipation due to the rotational drag can be estimated to be compared with the other two estimates. The energy dissipated inside the nuclear channel was estimated to be of the order of $1\times10^{-8} ergs$ ($1\times10^{-15} J$).

The rate of energy dissipation outside the head can be estimated by calculating the hydrodynamic drag force exerted on a cylindrical rod moving parallel to its long axis in an unbound fluid and multiplying the force by its velocity, $\dot{E} = F_{drag}v$. As given in Eq.(2.4) and Eq.(4.6), $F_{drag} = \zeta_{\parallel}vx(t) = 2\pi\mu x(t)v/[ln(L/2r) - 0.2]$, where $\zeta_{\parallel}$ is a translational drag coefficient per unit length parallel to its long axis, v is again the velocity of the acrosomal reaction (15μm/s), μ is the viscosity of the medium (water in our case) (10^{-3}kg/m·s), and r is the radius of the bundle (0.035μm). We use $x(t)$ instead of L, the total length of the actin bundle, since the length of the bundle experiencing the drag changes in time. Therefore, the energy dissipation outside the sperm head can be obtained as

$$E = \int_0^t \dot{E}dt' = \int_0^t F_{drag}vdt' = \int_0^t \zeta_{\parallel}v^2x(t)dt' = \int_0^t \zeta_{\parallel}v^3t'dt' = \frac{\zeta_{\parallel}v^3t^2}{2} \qquad (3.15)$$

where we used $x(t) = vt$. A typical velocity of the reaction v=15m/s, t=4s, and μ=10^{-3}kg/ms, yield the energy dissipation outside the head to be approximately 2.7×10^{-10}ergs (2.7×10^{-17}J).

We should also consider a case where the bundle is moving very near the surface rather than in an unbounded fluid. As discussed in chapter 2, this is the case similar to our experimental condition where most of velocity measurements were done on the sperms reacting near the surface. The average distance between the surface and the acrosomal bundle [1] lies between 1 and 3 μm. For an infinitely long cylinder moving near surface, the drag coefficient is given in Eq.4.5 as $\gamma_{\parallel} = 2\pi\mu L/\cosh^{-1}(h/r)$, where h is the the distance from the surface [24]. For the bundle moving near the surface, hydrodynamically dissipated energy is estimated to be 4×10^{-10} ergs (4×10^{-17}J), which is larger than the unbounded medium case, as expected.

$E_{inside} \geq 40\ E_{outside}$ and thus our assumption that most of energy is dissipated inside the nuclear channel was in fact valid. The difference in the dissipated energy inside the nuclear channel and in the medium will be even greater in reality owing to the fact that the viscosity of the cytoplasm is greater than that of water.

[1] The distance was measured first by focusing down at the surface on a slide with grids on, second by turning the focusing knob slowly until the acrosomal bundle comes in focus, and third by reading the increment off notch marks on the focusing knob.

Let us now consider the dissipated energy due to rotational drag. As mentioned in chapter 1, the actin bundle in its coiled state has 2.3 turns around its axis. Consequently, the extending bundle makes ~ 2.3 revolution per loop of the coil discharged. From the Fig. 1.4, we learned that the acrosomal bundle rotates as it extends, and its tip advances by $\sim 4.3\mu m$ for one revolution, which yields total $\sim$5023° rotation (15 revolution) for a $60\mu m$ long bundle. For a typical duration of the reaction, $4s$, the average value of the angular velocity, ω is $\sim 6\pi^c/s$. The drag torque per unit length for a rod rotating about its axis with angular velocity ω un an unbounded fluid, T/L is,

$$\frac{T}{L} = \zeta_r \omega = 4\pi\mu r^2 \omega \tag{3.16}$$

where ζ_r is the rotational drag coefficient per unit length for a axially rotating cylinder in unbounded fluid (See Fig. 4.2(b)) [57]. For a rod rotating about its axis near the surface

$$\frac{T}{L} = \gamma_r \omega = \frac{4\pi\mu r^2 \omega}{[1-(r/h)^2]^{1/2}} \tag{3.17}$$

where γ_r is the rotational drag coefficient per unit length for a circular cylinder rotating about its long axis near the wall (See Fig.4.2(a)) [24]. Since the $R \ll h$, the denominator is ~ 1, which yields the same equation as that of the unbounded fluid case. Then, using the parameter values given in foregoing analysis, the rate of energy dissipation is

$$\dot{T} = \gamma_r \omega^2 \text{ or } \zeta_r \omega^2 \approx 6.7 \times 10^{-19} J/s.$$

Total energy loss due to rotation is $E_{rot} \approx 3.4 \times 10^{-18}$J (or 3.4×10^{-11}ergs). This is about three orders of magnitude smaller than the dissipated energy inside the nuclear channel. Therefore, it was in fact a valid assumption to neglect the effect of rotation.

Chapter 4

Estimation of the acrosomal process bending stiffness using hydrodynamic flow: steady deflection mode

4.1 Introduction

We have learnt that the energy involved in the acrosomal process can be obtained by calculating the strain energy stored in the coiled state of the actin bundle. Equation 3.1 describes how much strain energy is stored in its bent and twisted structure of the coiled bundle, given the geometry of the coil and the material properties of the bundle. In Chapter 3.1, we estimated a bending stiffness, EI, by utilizing the scaling analysis which requires only appropriate units of each variable. However, the bending stiffness can vary by as much as three orders of magnitude when the chosen length scale λ is changed from 10μm to 60μm, for example. It is now desired to extract a closer approximation of the material properties by performing a thorough theoretical analysis along with the experimental studies.

Two modes of experiments and appropreaite analysis were carried out using the hydrodynamic flow. First mode is the *decaying mode* and the second mode is the *steady deflection mode.* In the decaying mode, the bending stiffness of an elastic rod can be estimated to relax back to its straight conformation. Whereas, in the steady deflection mode, we obtain the bending stiffness by relating the deflection of

a clamped beam with a known hydrodynamic drag force. In this chapter, we will only discuss experimental and theoretical analysis for the steady deflection mode as it is proven to yield more accurate result. The former mode will be discussed in the Appendix A.

4.2 Theoretical analysis

Here, we consider a long cylindrical rod moving through a viscous medium. This analysis again is in the low Reynolds number regime where the dynamics are dominated by the viscous effect; $Re \approx 10^{-8}$, based on the average diameter of the acrosomal bundle ($\sim$ 70nm) and the typical velocity of the acrosomal reaction ($\sim 15\mu$m/s).

We can estimate the bending stiffness of the acrosomal bundle by analyzing its bending shape at equilibrium in a steady hydrodynamic flow. First, the acrosomal bundle was considered as a elastic rod of length L with a circular cross section of radius r. We consider the acrosomal bundle lying perpendicular to the direction of the flow. When there is no motion in the fluid, the bundle remains at its initial equilibrium state, where it features the straight form. When the bundle, that is anchored on one end with the other end being free, is subject to a constant steady load exerted by a flow in the flow channel, it will bend along the direction of the flow to its new equilibrium deflection. While the flow is steady, the equilibrium shape of the bent bundle will remain at $y = y_0$. At this new equilibrium, the internal stress in the acrosomal bundle balances the external hydrodynamic force.

4.2.1 Elastic restorative force

As a rod bends in the viscous medium, the hydrodynamic drag force must be balanced by a restorative force exerted by the elastic nature of the rod as described in Fig. 3.1. The bending moment M depends linearly on the curvature κ of the rod, and thus for any angle θ along the bent rod, the bending moment of the beam becomes,

$$M = EI\kappa = EI\frac{\mathrm{d}\theta}{\mathrm{d}s} = EI\frac{\mathrm{d}^2y/\mathrm{d}x^2}{\sqrt{\left(1+(\mathrm{d}y/\mathrm{d}x)^2\right)^3}},$$

For small $\theta \ll 1$,

$$M \approx EI\frac{\mathrm{d}^2y}{\mathrm{d}x^2} \tag{4.1}$$

where we used the fact that the curvature κ is the derivative of the tangent angle θ with respect to the arc length s and that $x \approx s$, $\mathrm{d}y/\mathrm{d}x \approx \mathrm{d}y/\mathrm{d}s = sin\theta \approx \theta$, and $\mathrm{d}^2y/\mathrm{d}x^2 \approx \mathrm{d}\theta/\mathrm{d}s$ for small deflections (See Fig. 4-1). Figure 4-1(b) represents force and moment components in a small segment of the rod. Balancing the moments and forces yields the relationships between f_{drag}, shear forces V, and bending moments M as follows.

$$\begin{aligned} \frac{dM}{dx} + V &= 0 \\ \frac{dV}{dx} + f_{drag} &= 0 \end{aligned} \tag{4.2}$$

Combining Eq. (4.1) and (4.2), we obtain,

$$f_{drag}(x) = \frac{\partial^2 M(x)}{\partial x^2} = EI\frac{\partial^4 y(x)}{\partial x^4}. \tag{4.3}$$

EI is the bending stiffness of the bundle, and x and y are the coordinates defined in the Fig.A-3 as the long axis of the bundle and the axis perpendicular to the long axis, respectively.

The appropriate boundary conditions are those for the clamped-free beam given in Eq. A.16 (see A.2.4 for detail). At clamped end, $x = 0$, where there should be neither displacement nor slope allowed, the boundary conditions are

$$\begin{aligned} y(0,t) &= 0 \\ \frac{\partial y(0,t)}{\partial x} &= 0 \end{aligned}$$

while at $x = L$, the end is free with bending moment and shear force being equal to zero.

$$\begin{aligned} \frac{\partial^2 y(L,t)}{\partial x^2} &= 0 \\ \frac{\partial^3 y(L,t)}{\partial x^3} &= 0 \end{aligned} \tag{4.4}$$

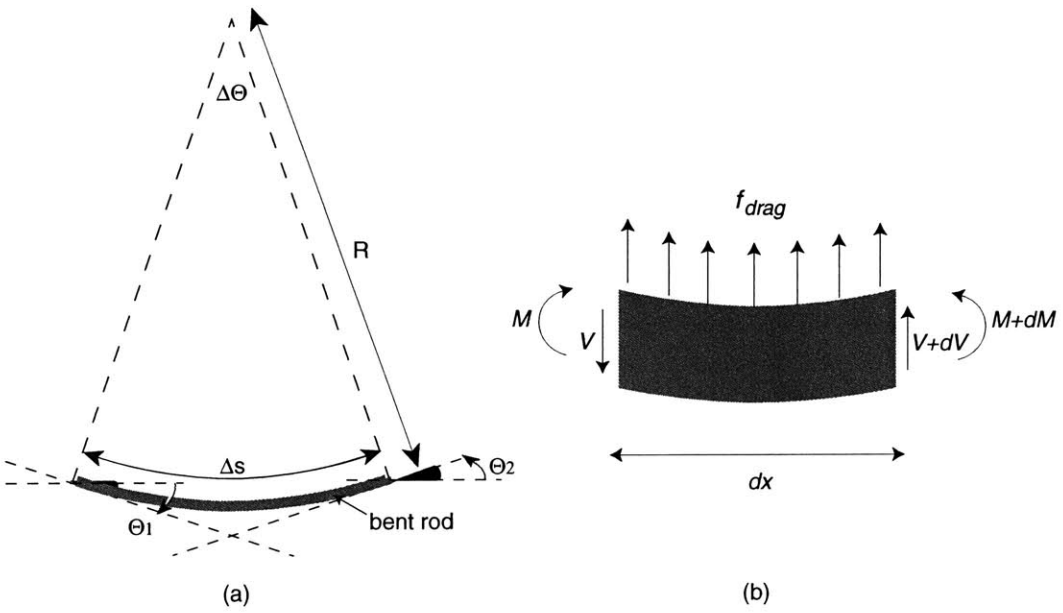

Figure 4-1: (a) Geometry of a bent rod: Over the arc length Δs, the corresponding increase in tangent angle is $\Delta\theta = \theta_2 - \theta_1$. The radius of curvature is then equal to the change in tangent angle with respect to arc length s for small angles. (b) Force and moment components of a small segment in the rod. By balancing the forces and moments, we can obtain $d^2M/dx^2 = f_{drag}$. V: shear force, M: bending moments

First, Eq. 4.3 is integrated 4 times to yield the solution in the following form;

$$y(x) = \frac{f_{drag}}{24EI}(x^4 + C_1x^3 + C_2x^2 + C_3x + C_4$$

By substituting the given boundary conditions in Eq. 4.4, we obtain the values for $C_1, C_2, C_3, andC_4$ and the expression for the shape $y(x)$ of the bent acrosomal bundle.

$$y(x) = \frac{f_{drag}L^4}{24EI}\left[(\frac{x}{L})^4 - 4(\frac{x}{L})^3 + 6(\frac{x}{L})^2\right] \tag{4.5}$$

4.2.2 Hydrodynamic drag force

Let us now consider the hydrodynamic drag force, f_{drag} on a bent rod (See Fig. 3-1). The acrosomal bundle remains in a plane parallel to the surface of the flow channel and thus, we assume that the velocity field of the flowing fluid is exerting a uniform force f_{drag} along the length of the bundle. f_{drag} can be related to the properties of the flow and the fluid viscosity. Since the viscosity of the water μ is known and the

velocity, v, of the flow can be measured by tracing the moving particles in the flow, we can obtain the hydrodynamic load on the acrosomal bundle by utilizing the equation for the hydrodynamic drag force per unit length

$$f_{drag} = \zeta v \tag{4.6}$$

where ζ is the drag coefficient. Venier et al (1994) discusses in the erratum two possible definitions of the friction coefficient (which we call the *drag coefficient* in this thesis. "The first corresponds to the case of the filament movement relative to the surface, relevant to the active transport of filaments. This friction coefficient is a function of the distance between filament and surface. The second corresponds to the flow of fluid past a filament *stationary* with respect to the surface. In this case the modifications of the friction coefficient are small compared with the uncertainties of the positions of the filament [58]." The steady deflection mode we are dealing with is that of the latter case where the flow is moving while the bundle is stationary with respect to the surface. Therefore, unlike the case of the decaying mode analysis, we will use the drag coefficient ζ for a long slender rod at rest in a moving fluid. The appropriate drag coefficient is [5]

$$\zeta = \frac{4\pi\mu}{\ln(L/d) + 2\ln 2 - 1/2} \tag{4.7}$$

where L is the length of the bundle and d is the diameter of the bundle. Given these, our hydrodynamic force per unit length takes the form

$$f_{drag} = \frac{4\pi\mu v}{\ln(L/d) + 2\ln 2 - 1/2} \tag{4.8}$$

Now our final solution corresponding to the bent acrosomal bundle can be rewritten in the following form

$$y(x) = \frac{\pi\mu v L^4}{6EI(\ln(L/d) + 2\ln 2 - 1/2)}\left[(\frac{x}{L})^4 - 4(\frac{x}{L})^3 + 6(\frac{x}{L})^2\right] \tag{4.9}$$

The value of the bending stiffness EI can be derived by adjusting the theoretical curve from Eq. 4.9 to the experimental curve.

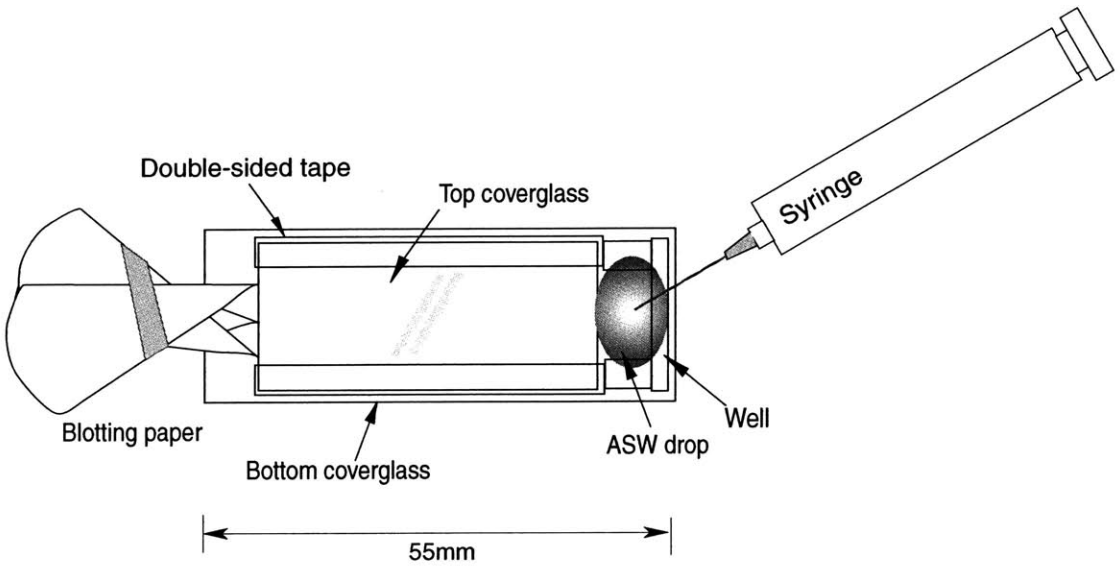

Figure 4-2: A schematic of a flow channel for the steady deflection experiment.

4.3 Experimental analysis

4.3.1 Experimental setup and sample preparation

We followed the same procedure as in 2.4.4. Briefly, 500μ sperms were collected from a selected crab, and the collected sperms were washed twice by centrifugation. The washed pellet was resuspended in ASW to its original volume, and kept on ice at all times.

All experiments are carried out with a flow channel whose both ends are left open for easy injection of buffer. This is the similar flow channel used for the temperature dependence experiment described in section 2.2.1 except that this features a longer channel than the previously used one (see Fig. 4-2). A longer flow channel was desired so that at least the mid-region of the flow channel would be kept away from any possible turbulence effects generated as the fluid was being added and drawn at the entrance and exit area of the channel.

Sperms were added to the flow channel and the calcium ionophore (A23187) was added once the sperms were settled down on the surface. We then selected those

reacted sperms initially lying perpendicular to the direction of the flow (before the flow was applied). Using a pipette, 300ml of 25mM $CaCl_2$ ASW in added in the well on one end of the channel. As described in Fig. 4-2, a little well was made with double-sided tape and pieces of cut plastic coverslips (18mm× 18mm). Due to the surface tension of the liquid, which keeps liquid drop in a spherical shape, the drop of the liquid remains in the well. When ready, we let a bundle of 3 slices of the blotting paper (54 Hardened 90mm Circles (Whatman, Inc) were cut in 6 slices) touch the liquid from the other end of the flow channel. We made a bundle for two reasons: First, it was to increase the flow velocity by increasing the absorbing capability and secondly to generate a distributed drawing of the liquid rather than a localized removal, as this may affect the velocity distribution inside the flow channel. While the blotting paper was absorbing the liquid from one side, ASW drops were constantly added on the other side by holding the 21G syringe needle (with 10ml syringe filled with ASW) above the well and letting the liquid drip from the needle at a more or less same rate.

4.3.2 Light microscopy and data analysis

The acrosomal bundles were observed in Nikon Eclipse TE300 inverted microscope equipped with a Nikon plan apo-60X DICH oil immersion objective lens (numerical aperture (N.A.) 1.4). Images were acquired with a Dage MTI camera (Model CD-300-RC) , and recorded with a Sony SVO-9500MD Super-VHS video recorder. The images were then digitized using the Apple video player (Apple computer, Inc), a software that allows us to convert the video-taped images to QuickTime movies at a video rate, 30 frames per second. Although the quality of the digitization with the Apple video player is less than that with the Openlab timelapse along with the Snapper framer grabber, it has its merit of being able to digitize images at a full video rate. To measure the velocity of the fast moving particles, 10 fps (frames per second) rate did not yield enough measurements. Two different measurements were performed, namely the particle velocities to estimate the flow velocity and the displacement of the tip. The procedures are described in detail in the following section. Measurements

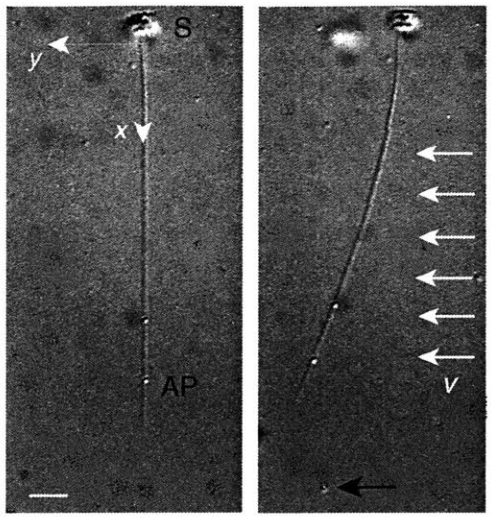

Figure 4-3: Images of the acrosomal process subject to a hydrodynamic flow. (a) In the absence of flow, the acrosomal bundle exhibits a straight shape. S: sperm head, AP: the acrosomal process (b) When the flow is applied perpendicular to the axis of the acrosomal bundle, it bends to its new equilibrium state. The flow velocity was estimated by following the particles and it was 120μm/s for this particular bundle deflection. A black arrow locates the particle. White arrows indicate the direction of the flow. The scale bar measures 5μm.

were saved as a mat file format and plotted using Matlab (The Math Works, Inc).

4.4 Results and discussions

4.4.1 Evaluation of fluid flow velocity and its stability

As described in the previous section, the acrosomal bundle of the reacted sperm was forced to bend by a fluid flow in the flow cell. In this experiment, it is necessary that the flow is steady. In other words, the deflection of the bundle we are observing should correspond to its equilibrium state not some transitional state. In order to verify the steadiness of the flow, we did two different measurements. First, we measured velocity of the particles moving along the flow. Since the particle sizes are small (0.5-2.5μm in diameter) and they appear to move along the flow, we assume that the velocity of the particle is same as that of the flow. Second, the deflected distance of the tip at equilibrium was measured for about 4-7 seconds in average. If the flow is indeed steady, we should expect constant velocities for the particles and a constant

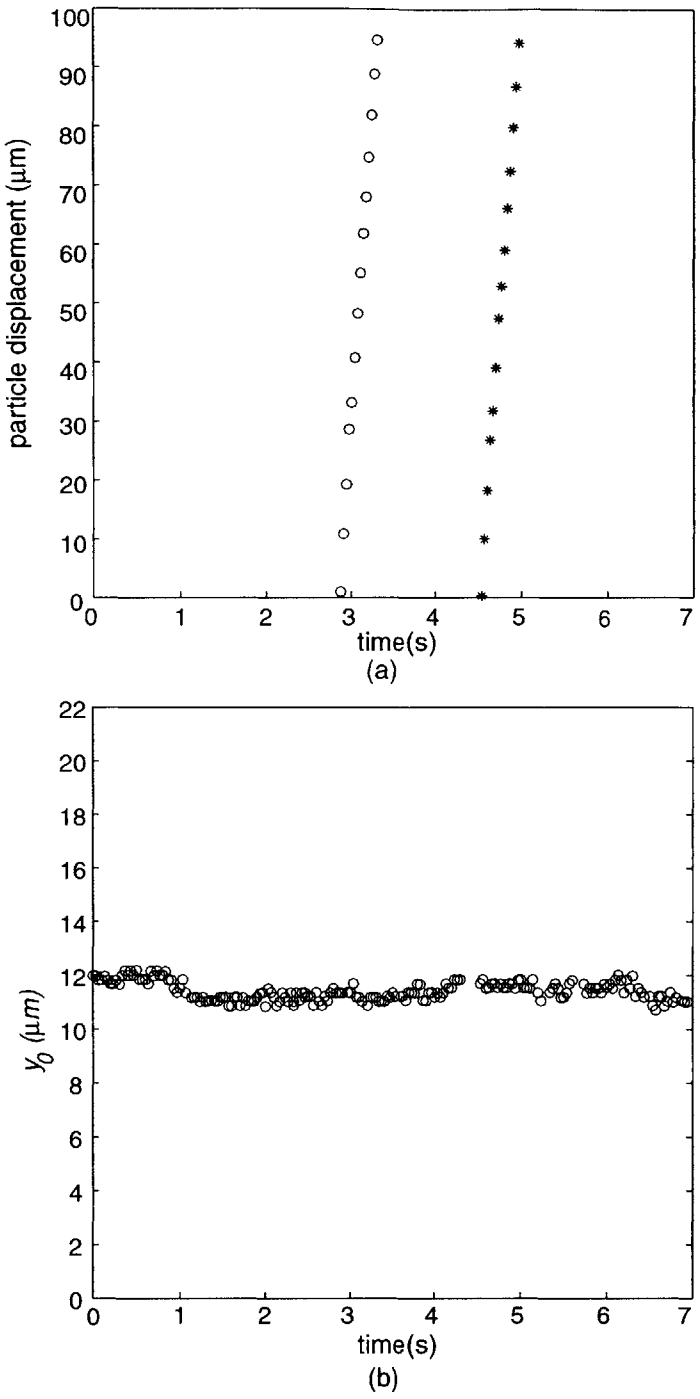

Figure 4-4: (a) A plot of particle velocity: In this particular case, there are two particles moving along the flow during the period of observation. The velocity of the particles are constant over time. (b) A plot of the acrosomal bundle tip displacement over time. From these two observations, a constant particle velocity and a constant tip displacement, we can make sure that the flow has reached its steady state.

displacement of the tip over the given period. The velocity was evaluated by recording the movement of particles moving in the same focal plane as the relaxing acrosomal bundle. As seen in Fig. 4-4(a) is a typical velocity profile of the particles and (b) is one for displacement of the tip. This suggests that we were able to generate a steady flow in the flow channel and our theoretical analysis is valid and compatible with the experimental data. Results from 8 acrosomal bundles are listed in Table 4.1.

4.4.2 Results

As shown in Fig. 4-3, the acrosomal bundle exhibits a straight shape in the absence of flow, and it bends to its new equilibrium state when a hydrodynamic flow is applied. From the images of the bent acrosomal bundle, we took about 30-40 points of the bundle positions at different (x, y) along the bundle. The value of the bending stiffness EI can be obtained directly by adjusting the theoretical curve from Eq. 4.30 to the experimental curve. A typical result is shown in Fig. 4-5 where the circles represent the experimental data and the dashed line is a theoretical curve calculated according to Eq. 4.30 with $L = 49.5\mu$m, $\mu = 10^{-3}$kg/sm, $d = 70$nm, $v = 120\mu$m/s, and $EI = 1.4 \times 10^{-20}$Nm^2. The average EI value obtained from 8 acrosomal bundle was 1×10^{-20}Nm^2 with the standard deviation of 0.5×10^{-20}Nm^2. A complete list is again shown in Table 4.1.

4.4.3 Discussion

As a comparison, the average bending stiffness estimated from the decaying mode experiment (see A.3.1) was 1.6×10^{-21} while the one estimated by steady deflection mode is 1×10^{-20}, one order of magnitude greater. This suggests that we must have underestimated the bending stiffness in the decaying mode by disregarding the presence of the residual flow. In other words, the residual flow was most likely delaying the relaxation of the bundle, leading us to underestimate the EI by having longer relaxation time.

On the other hand, the EI value obtained from the steady deflection analysis is the same order of magnitude as our priliminary estimation presented in Chapter

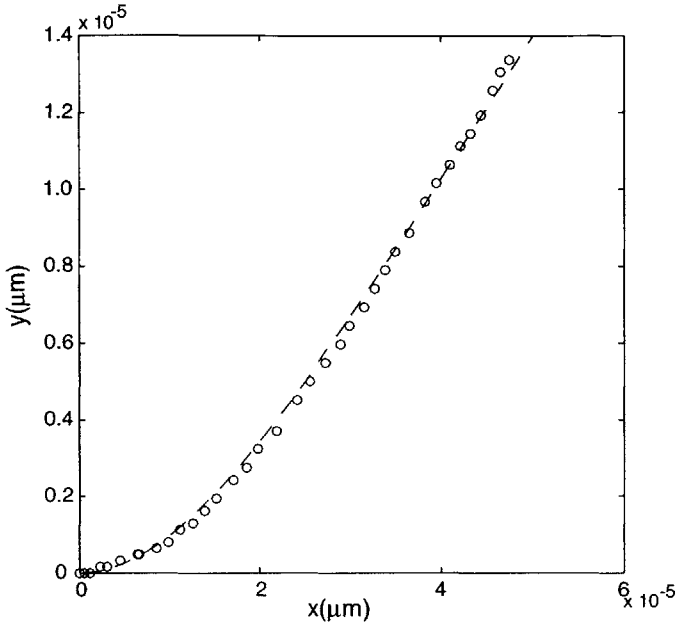

Figure 4-5: Comparison between the theoretical curve and the experimental data of the bent acrosomal bundle in a steady flow. y represents the deflection from the straight state of the bundle and x is the position along the bundle. The origin lies at the base of the sperm head as indicated in Fig. 4.3. The circles represent the experimental data and the dashed line is a theoretical curve calculated according to Eq. 4.30 with $L = 49.5\mu$m, $\mu = 10^{-3}$kg/m$\times$s, $d = 70$nm, $v = 120\mu$m/s, and $EI = 1.1 \times 10^{-20}$Nm^2.

3, which is $\approx 1 \times 10^{-20}$Nm^2. As a comparison, the bending stiffness of an individual actin filament is approximately 7.3×10^{-26} Nm^2. Considering that the acrosomal bundle is made of upto 80 actin filaments and the bundle features a helical structure, our estimate seems to lie in a reasonable range. Also, based on this EI value of the acrosomal bundle, the energy initially stored in the coil is calculated to be $7 \times 10^{-6} ergs$.

Table 4.1: Bending stiffness of the acrosomal bundle derived from their bending shape in a hydrodynamic flow. The tip deflection was measured from its straight shape. The flow velocity was estimated by measuring the particle velocity. The bending stiffness was derived from the analysis of the bending shape of each acrosomal bundle of a given length in a steady flow.

Length	Tip deflection	Flow velocity	Bending stiffness
μm	μm	μm/s	$\times 10^{-20}$Nm^2
49.5	11.5	120	1.1
49.5	11	45	0.6
49.5	11.1	85	1.0
47.5	2.9	14.5	1.1
49.9	6.2	125.9	2.7
50.6	7.5	62.3	1.6
50.3	4.6	47.5	1.4
51.4	21.9	130	0.8

Chapter 5

Conclusion and proposed future works

We have investigated the dynamics of the acrosomal process in the sperm of *Limulus polyphemus* which involves a very unique way of generating force - by storing mechanical potential energy and converting it into translational work. This unusual form of motility is worth studying because it features a novel mechanism of actin based motility where the mechanics and the chemical kinetics are coupled. In this chapter, the contents of the thesis are summarized followed by a few comments on future directions.

5.1 Summary of research

We first examined the uncoiling mechanism of the initially coiled actin bundle to its straight comformation. The evolution of the acrosomal process was followed using video microscopy, to find the velocity of the reaction being constant over time. This is consistent with the zipper-like model where a localized uncoiling of the actin bundle propagates along the bundle. The average velocity of the acrosomal process depends on the temperature of the environement and increases as the temperature is raised, varying from approximately 37 μm/s at 32°C to 1.7 μm/s at 9.6°C. The morphological dependence of the reaction rate was then investigated by electron micrograph studies. The collected sperms from various crabs shared common mophological features despite the differences in their average reaction velocities. The effects of external load was

also studied by varing the viscosity of the medium through which the acrosomal bundle extends. Results exhibited a negative correlation between the viscosity of the medium and the extension velocity.

Based on dynamical measurements of the uncoiling and the extension of the actin bundle, we estimated the energy stored in the coiled state of the acrosomal bundle as well as the energy dissipated during the extension. We first estimated the hydrodynamic energy dissipation during the reaction. This provides us a lower bound estimate of the initial energy required for the acrosomal reaction to occur, and was approximately 10^{-8}ergs. Initially, the acrosomal bundle stores a mechanical strain energy in its coiled state which is released during the extension process. There also exists some energy involved in Ca^{2+} binding to calmodulin during the reaction. Estimation of the mechanically stored energy requires the mechanical properties and the geometry of the bundle to be known. The bending stiffness of the acrosomal bundle was measured by applying a steady flow on an initially straight actin bundle lying perpendicular to the flow direction. The bundle was modeled as a clamped rod subject to a constant load along the bundle, and its deflection was correlated with the velocity of the steady flow to obtain the EI of 10^{-20}Nm^2. Given this estimate of the bending stiffness and known geometry, we estimated the intial energy stored in the bundle to be $7{\cdot}10^{-6}$ergs, which is more than two orders of magnitude larger than the hydrodynamically dissipated energy during the reaction. These results indicate that the bundle indeed behaves like a mechanical spring and the strain energy is the major source of the energy that powers the acrosomal reaction to completion.

5.2 Suggestions for future Work

5.2.1 Bending stiffness measurement using magnetic trap

There remain some questions for future consideration. First, we are currently extending the bending stiffness measurement experiment in collaboration with Jason Sutin in Professor Peter So's Lab at MIT. In Chapter 4, we managed to estimate the bending stiffness of the acrosomal bundle by utilizing a steady hydrodynamic

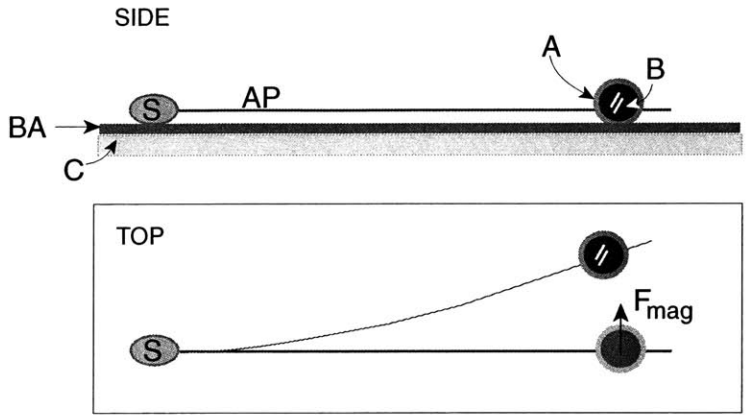

Figure 5-1: A schematic representation of the bending stiffness measurement with a magnetic trap. AP: the acrosomal process labeled with amine reactive biotin, B: magnetic bead coated with avidin (A) (biotin-binding protein), and S: sperm head anchored on the surface of coverslip (C) covered with a blocking aid (BA). When the magnetic force (of known value) is applied, the bead moves to bend the acrosomal bundle. By relating the shape of the deflection and the applied force, one can measure the bending stiffness of the bundle.

flow. This method assumes the particle velocity being equal to the flow velocity, which is a pretty good approximation as long as the particles are neutally buoyant. Also, the drag coefficient used in the solution is for a statoinary cylincer of a uniform cross-section in a moving fluid while in case, the cross-sectional area varies along the bundle. A better way would be a static experiment using a magnetic trap, which involves approximation of neither the drag coefficient nor the flow velocity. We can anchor one end of the acrosome whlie the other end is coupled with a magnetic bead. By applying a known magnetic force to the bead attached at the tip of the bundle, we can bend the bundle to y_0. This a case of a clamped rod with a concentrated load at the tip which can be expressed as

$$y(x) = \frac{f_{mag}x^4}{6EI}(3L - x) \tag{5.1}$$

where L is the length between the wall and the bead and f_{mag} is the magnetic force exerted by the trap. As one may notice, this involves only two values, the applied force and the shape of the deflection (See Fig. 5-1).

5.2.2 Calcium detection with confocal laser scanning microscopy

Next, detecting spatial and temporal distribution of Ca^{2+} in the course of the reaction is recommended. Although it has been known that calcium plays a very significant role in *Limulus* sperm acrosomal process, little study has yet been done on the mechanism of calcium binding to initiate the process in *Limulus* sperm. In chapter 2, we proposed the uncoilng mechanism to be that of a localized zipper-like mechanism, which was consistent with the extension profile in time obtained from the experiment. The localized conformation change in scruin may suggest presence of localized calcium channel or a regulator. Yet, no direct evidence has been provided. Studying the temporal and spatial distribution of intracellular Ca^{2+} in the *Limulus* sperm may provide us useful information which may serve as a direct evidence to explain the dynamics of the uncoiling. This spatiotemporal detection of Ca^{2+} can be done with Ca^{2+} imaging technique implementing confocal laser scanning microsopy. With two visible light-excitable fluorescent Ca^{2+} indicators, two-emission ratio imaging can be performed.

5.2.3 False discharge reaction

What we have discussed so far in this thesis was named by Andrè(1965) the *true discharge* as this is the essential true reaction in fertilization. There remains a fascinating process designated the *false discharge* in sperm, which is often extruded near the flagllum with an acute angle to it (See Fig. 5-2). When freshly collected sperms are diluted in artificial sea water, we may observe a part of the false dischage 3-25μm whose length depends of the condition of the buffer. Unlike the true discharge, the false discharge is helical. DeRosier described [8] that the bundle in both coiled and false discharge state is composed of straight segments and bends. The bundle is supercoiled in both cases but the degree of twist of the filament and hand of the supercoil differ. Unlike the TD, the FD is a reversible process. When excess Ca^{2+} (or Ca^{2+} ionophore) is added to solution, the false discharge retracts into the sperm head and the straight form of TD extends from the anterior end. When the sperms are treated with detergent (0.1%Triton-x100), the FD extends from its posterior end

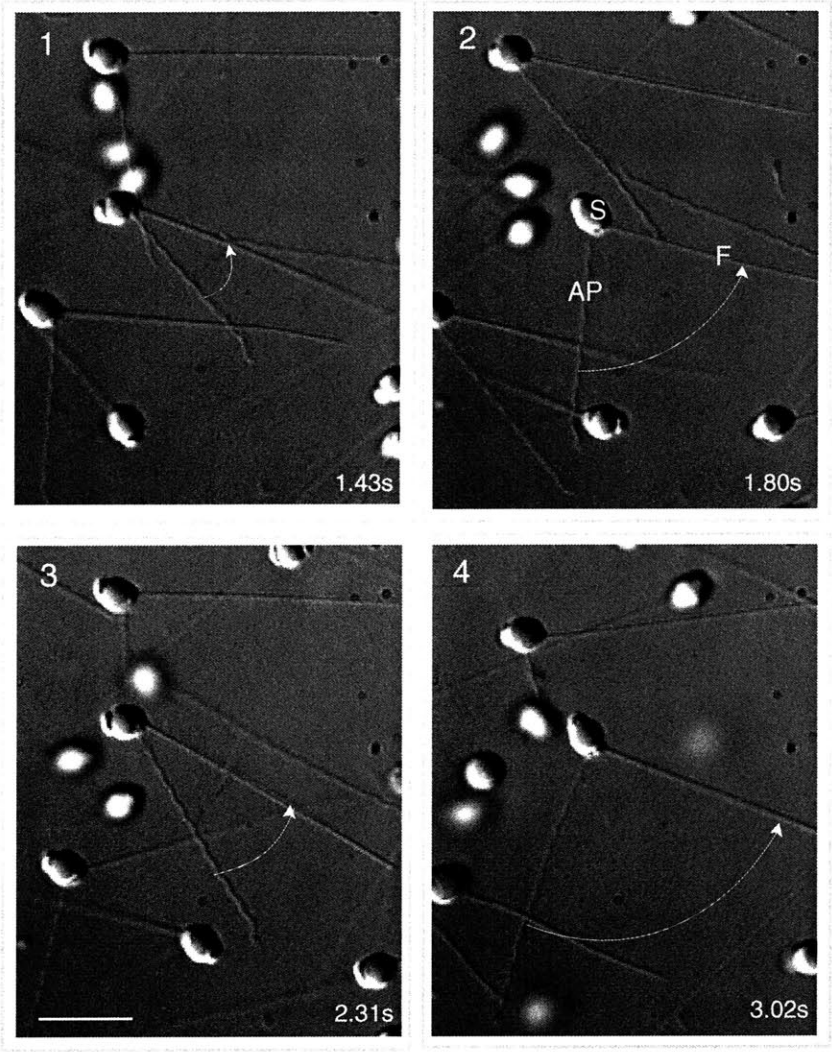

Figure 5-2: A sequence of extending false discharge (FD) reaction. One can observe a flapping motion of the FD as it extends out in 0.1% Triton X-100. S: sperm head, AP: the acrosomal process, and F: flagellum. Scale bar measures 10μm.

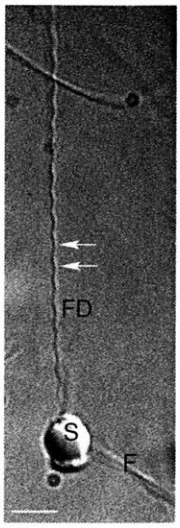

Figure 5-3: An image of a FD ($\sim$ 45μm long). The acrosomal process length between two arrows represents one period. Scale bar measures 5μm.

almost to it full length, which is about 45-50μm (See Fig. 5-3). Interestingly, in 0.1% Triton X-100 medium, the extended FD often retracts even in the absence of excess Ca^{2+} or ionophore. As described in Fig. 5-2, the extension and retraction of the FD go through a series of flapping motion. For a full length FD ($\sim$ 45-50μm), there exist about 5-6 flapping cycles. For each cycle, $\sim$ 3-3.5 periods of helix extrudes out. This flapping of the FD may correspond to the unpacking and packing into a coil.

As done in the case of the TD, we would like to investigate the uncoiling mechanism of the FD from the coiled state. We will then study how the higher ionic strength and the presence of detergent induce the extrusion of the FD. The extension and retraction rate can be determined by measuring the extension distance in time from the images taken using the high speed camera. Correlation between the reaction rate and the experimental conditions such as temperature, ionic strength, and detergent concentration is to be determined as well. We will study the relationship between the reversibility and the energy involved during the conversion from one state to the other (Coiled state and FD state).

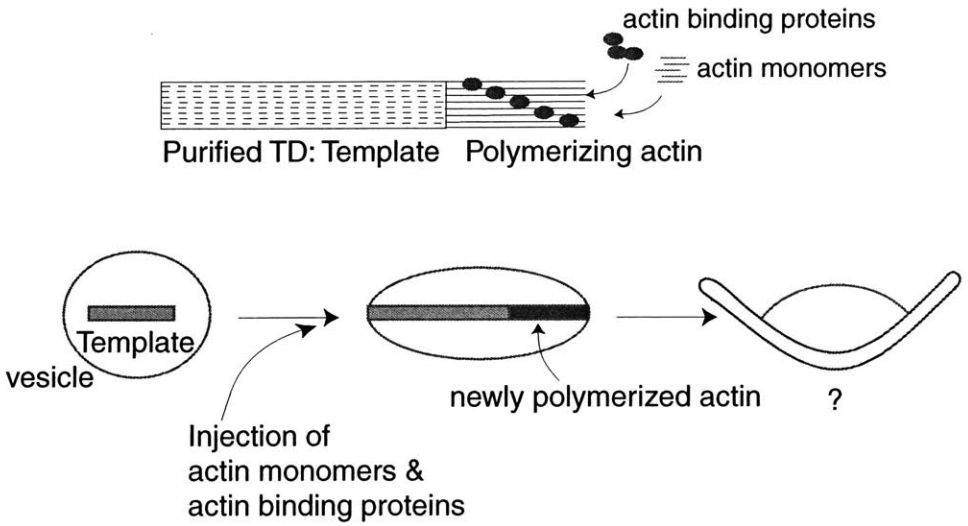

Figure 5-4: Force measurement experiment of the polymerizing actin bundle.

5.2.4 Actin polymerization

Measuring force generation in polymerization

In collaboration with John Eundamrong and the Mitchison lab at Harvard Medical School, we are interested in measuring the force generated during the polymerization of actin. From a pool of actin monomers and actin bundling proteins such as scruin, fambrin, and fascin, we can polymerize a long bundle of highly organized actin filaments. Miyata and Hotani have observed morphological changes in liposome caused by polymerization of encapsulated actin [35]. D. Fygenson measured force generated as encapsulated microtubules buckle to deform lipid vesicles [17]. Thus, we may utilize their observations and experimental techniques to measure the force generated by growing actin bundle inside a lipid vesicle. To construct an actin bundle like that of the true discharge, we can also use fragments of purified true discharge as templates along with actin monomers and scruin. There arise few issues to consider in attacking these experiments such as a controlled mechanism of the assembling and disassembling of the actin bundle and a suitable protocol to encapsulate the actin monomer and actin binding proteins (See Fig. 5-4).

Bundling effect of few actin binding proteins

Another interest lies in measuring the bending stiffness (or often called *flexural rigidity*) of the actin bundle cross-linked with different actin bundling proteins such as scruin, fimbrin, or fascin. Results from these measurement will tell us the difference in bundling effect of each actin bundling protein.

Appendix A

Estimation of the acrosomal process bending stiffness using hydrodynamic flow: decaying mode

We will first examine how the time constant can be derived and applied to predict the bending stiffness of an elastic rod. Following the analysis, we will introduce an experiment where a simple hydrodynamic flow is used along with high resolution microscopy to measure the decaying time of the initially bent acrosome bundle. Lastly, the steady deflection experiment procedure will be discussed along with the solution to the elastic beam equation.

A.1 Theoretical analysis

A.1.1 Hydrodynamic drag force

Here we consider a long cylindrical rod moving through a viscous medium. This analysis again is in the low Reynolds number regime where the dynamics are dominated by the viscous effect; $Re \approx 10^{-8}$, based on the average diameter of the acrosomal bundle ($\sim$ 70nm) and the typical velocity of the acrosomal reaction ($\sim 15\mu$m/s).

The motion of an elastic rod in a viscous fluid is predicted by balancing the hydrodynamic drag force exerted on the relaxing bundle and the elastic restoring force of the bundle. Let's first consider the hydrodynamic drag force on a bent rod

(See Fig. 3-1), which can be written as

$$f_{drag}(x) = -\zeta_{\perp}\frac{\partial y(x)}{\partial t} \tag{A.1}$$

where $\zeta_{\perp}$ is a translational drag coefficient normal to the long axis (for transverse motion). Here we should note that Eq. 4.1, the drag force equation, is based on the fact that the rod exhibits an overdamped response and the bending is not too large, so that the small angle approximation in the velocity term is still valid.

How do we get the drag coefficient, ζ, for a long cylinder moving in a viscous medium? First, the drag coefficient is simply $\zeta = F/v$, and thus v and F must be known in order to find the value of ζ . By solving the Navier-Stokes equation with appropriate boundary conditions, one can derive an expression for the flow velocity, u. A flow in a low Reynolds number regime, the acceleration $D\mathbf{u}/Dt$ is so small compared to the viscous force per unit mass $\nu\nabla^2\mathbf{u}$ at each point of the fluid that we may neglect it in the Navier-Stokes equation given in Eq. 3.4. This kind of flow having a very low Reynolds number is called a *Stokes flow* or a *creeping flow*, and the equation of motion takes the following form, along with the mass conservation equation :

$$\mu\nabla^2\mathbf{u} = \nabla p$$

$$\nabla \cdot \mathbf{u} = 0. \tag{A.2}$$

For the one-dimensional problem such as a long centrally located cylinder moving axially inside a larger cylinder (See chapter 3.3), the governing equation takes the form of

$$\frac{1}{r}\frac{d}{dr}(r\frac{du_z}{dr}) = \frac{1}{\mu}\frac{dp}{dz}$$

and u_z can be found as shown in Eq. 3.14 with given boundary conditions in Eq. 3.10, 3.11, and 3.12 (See. Fig. 3.2). Once u_z is found, one can calculate the drag coefficient ζ from the expression of f_{drag} per unit length,

$$f_{drag} = 2\pi\mu r_2[\frac{dv}{dr}]_{r=r_2} = \zeta v$$

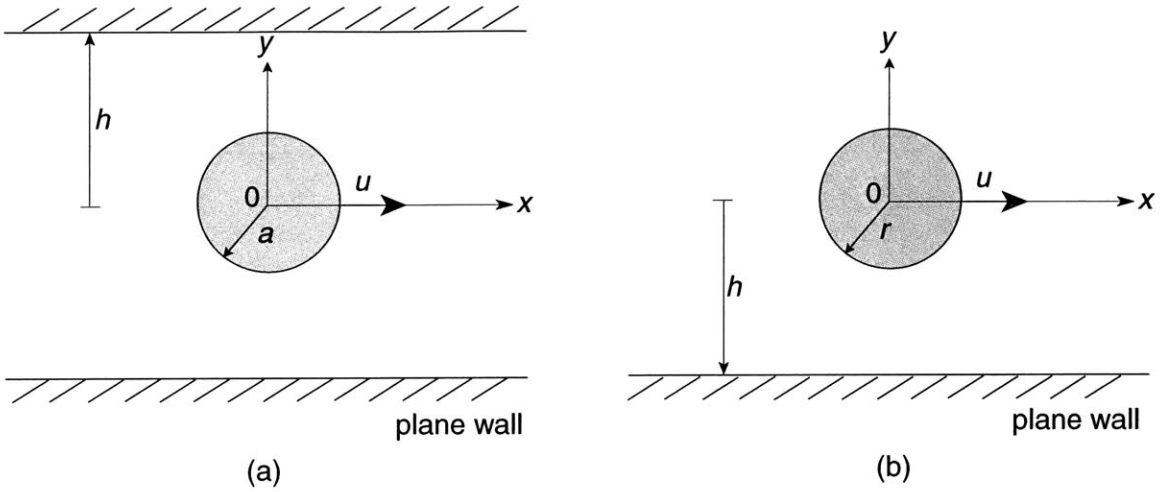

Figure A-1: Definition drawings of a cylinder moving (a) midway between two parallel walls and (b) near a single plane wall.

where v is the velocity of the moving inner cylinder. For a limited case of $r_o \gg r_i$, the ζ_{cc} is found to be

$$\zeta_{cc} = \frac{2\pi\mu}{\ln(r_o/r_i) + 1} \tag{A.3}$$

for the axially moving slender cylinder inside a tube [23]. r_o, r_i, and μ are the radius of the outer cylinder, that of the inner cylinder, and the viscosity of the medium, respectively.

For the two-dimensional flow with an infinitely long cylinder moving perpendicular to its axis in the midway between two parallel plane walls $2h$ away from each other (See Fig. A-1(a)), Takaisi [50] obtained a drag coefficient per unit length to powers of (a/h^4) based on the Oseen's linearized equation of motion. For a limiting case of $h \gg a$, ζ_{dw} becomes

$$\zeta_{dw} = \frac{4\pi\mu}{\ln(h/a) - 0.9156} \tag{A.4}$$

Takaisi also considered the problem of motion of a circular cylinder parallel to a single plane wall when the cylinder is moving perpendicular to its own axis (See Fig.A-1(b) [51]. He only obtained a solution in the limiting case of $r \gg h$ where r is the radius of the cylinder and h is the distance between the cylinder axis and the wall, and it was found to be

$$\zeta_{sw} = \frac{4\pi\mu}{\ln(2h/r)}.$$

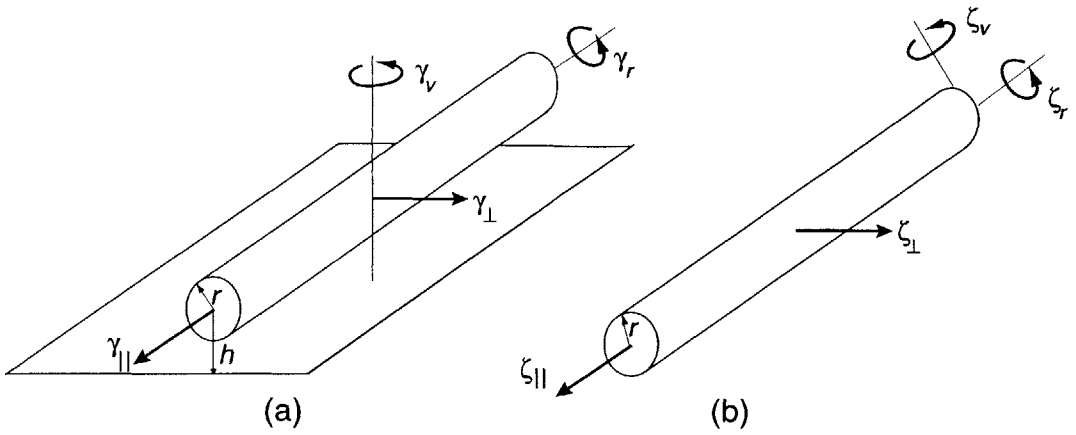

Figure A-2: Drag coefficients for a cylinder moving (a) near a plane wall (b) in an unbounded fluid.

More general solution for the drag coefficient for this problem, which is similar to what we will be dealing with in our decaying mode experiment, was provided by Jeffrey and Onishi by deriving an exact solution to the Stokes equation[24]. From here on, I will denote the drag coefficients per unit length for a cylinder moving near the single plane wall, γ (See Fig.A-2(a)).

$$\gamma_\perp = \frac{4\pi\mu}{\ln\{(h/r) + [(h/r)^2 - 1]^{1/2}\}} \tag{A.5}$$

For a long cylinder of length l and radius r in an unbounded fluid (Fig. A-2(b)), exact solutions to the Stokes equation do not exist [20]. Tirado and Garcia de la Torre [56] solved for the approximated translational friction coefficients (ζ) in unbounded viscous medium by modeling the cylinder as N_r stacked rings while N_r is the number of rings. This represents the case of the acrosomal bundle extending in the unbounded medium outside the sperm head where there exists a hydrodynamic drag parallel to the axis of the bundle. The drag coefficient for a cylinder moving parallel to its long axis with a correction term for the end effects is given by Torado as

$$\zeta_\parallel = \frac{2\pi\mu L}{\ln(L/2r) + \alpha_\parallel}. \tag{A.6}$$

For the limiting case of $L/r \gg 1$, $\alpha_\parallel$ = -0.2 while the value of α depends on the shape of the body [28, 5, 6]. Other translational and rotational drag coefficients for

Table A.1: Drag coefficient per unit length for a long cylinder moving 1) near a single plane wall and 2) in unbounded fluid [20]. h represents the distance of the cylinder axis from the wall, r the radius of the cylinder, L the length of the cylinder, and μ the viscosity of the medium. Approximate values of the constant αs are $\alpha_{\parallel}$=-0.2, $\alpha_{\perp}$=0.84, and α_v=-0.662 [56, 57].

Boundary Condition	Orientation of the movement	Drag coefficient
Near a single wall	Translational movement: Parallel to its axis	$\gamma_{\parallel} = \frac{2\pi\mu}{cosh^{-1}(h/r)}$
	Translational movement: Perpendicular to its axis	$\gamma_{\perp} = \frac{4\pi\mu}{cosh^{-1}(h/r)}$
	Rotational movement: about its axis	$\gamma_r = \frac{4\pi\mu}{[1-(r/h)^2]^{1/2}}$
	Rotational movement: about an axis vertical to the wall	$\gamma_v = \frac{1}{(\gamma_{\perp}{}^{-1} - \gamma_r{}^{-1})}$
In an Unbounded fluid	Translational movement: Parallel to its axis	$\zeta_{\parallel} = \frac{2\pi\mu}{\ln(L/2r) + \alpha_{\parallel}}$
	Translational movement: Perpendicular to its axis	$\zeta_{\perp} = \frac{4\pi\mu}{\ln(L/2r) + \alpha_{\perp}}$
	Rotational movement: about its axis	$\zeta_r = 4\pi\mu r^2$
	Rotational movement: about an axis vertical to its axis	$\zeta_v = \frac{1/3\pi\mu L^2}{\ln(L/2r) + \alpha_v}$

a moving cylinder both near the wall and far from the wall are listed in Table A.1. the long axis, respectively.

A.1.2 Elastic restorative force

Now, as the bent rod relaxes through the viscous medium, the hydrodynamic drag force must be balanced by a restorative force exerted by the elastic nature of the rod. The external force per unit length, f_{drag}, acting at each point of the acrosomal bundle is given in Eq. 4.3 as

$$f_{drag}(x) = EI\frac{\partial^4 y(x)}{\partial x^4}$$

where EI is the bending stiffness of the bundle, and x and y are the coordinates defined in the Fig.A-3 as the long axis of the bundle and the axis perpendicular to

A.1.3 Net force acting on a bent elastic rod

By substituting Eq. A.1 into Eq. 4.3, we can obtain the elastohydrodynamic beam equation:

$$\frac{\partial^4 y(x,t)}{\partial x^4} = \frac{1}{EI}\frac{\partial^2 M(x)}{\partial x^2} = -\frac{\zeta_\perp}{EI}\frac{\partial y(x,t)}{\partial t}.$$

This equation represents that elastic forces characterized by a fourth order spatial derivative balance viscous drag and may be rewritten as

$$\frac{\partial^4 y}{\partial x^4} = -\frac{\zeta}{A}\frac{\partial y}{\partial t} \tag{A.7}$$

where A represents a bending modulus EI.

The solution to this equation can be obtained by separating our equation into a temporal term $T(t)$ and a spatial term $X(x)$, which satisfies $y(x,t) = X(x)T(t)$. This technique is called the separation of variables. We then obtain two equations,

$$\frac{\partial^4 X(x)}{\partial x^4} - \beta^4 X = 0$$

$$\frac{\partial T(t)}{\partial t} + \beta^2 \frac{EI}{\zeta} = 0 \tag{A.8}$$

where β is some constant which satisfies $X''''/X = -\zeta/EI(T'/T) = \beta^4$

The solution is then in the form of

$$y(x,t) = exp(-\frac{EI\beta^4 t}{\zeta})(c_1\, cos\, \beta x + c_2\, sin\, \beta x + c_3\, cosh\, \beta x + c_4\, sinh\, \beta x). \tag{A.9}$$

A.1.4 Initial condition and boundary conditions

Having a general solution to the governing equation, Eq. A.7, let us now consider appropriate boundary conditions and an initial condition. The detailed experimental setup will be discussed in the following section, but we must know the experimental conditions to figure out what are the most appropriate boundary and initial conditions for our analysis. As briefly mentioned in section 4.2.1, the sperm head is attached

Table A.2: Two possible boundary conditions for the acrosomal bundle extended out of the nuclear channel.

No.	End Condition	B.C. at $x = 0$	B.C. at $x = L$
I.	Clamped/Free	$y = 0, y' = 0$	$y'' = 0,\ y''' = 0$
II.	Linear Spring/Free	$k(y - y_\circ) + EIy''' = 0,\ y'' = 0$	$y'' = 0,\ y''' = 0$

to the surface of the flow cell while a free end of the $\sim 60\mu$m acrosomal process is relaxing from its initially bent configuration.

There are a couple of possible boundary conditions for this particular setup as microscopic detail is not known at the constrained end. As described in Fig. 4.4, one end of the acrosomal bundle is constrained by the presence of the nucleus surrounding the bundle. This appears to be akin to the *clamped* boundary condition. However, we do not know how the nucleus would behave when it is subject to a load on the bundle. First, we may assume that the nucleus behaves like a rigid wall and the acrosomal bundle is clamped in the wall so that the acrosomal bundle is not free to move or to rotate about its axis. This is called a clamped-free end condition. This boundary condition implies that there is neither a displacement nor a slope at the clamped end. Secondly, it is possible that the nucleus behaves like an elastic spring, and the end condition will be like a linear spring attached to a beam. Although it is possible, the second boundary condition is rather difficult to apply since the spring constant, k, of the nucleus is not known. Therefore, we will treat only the clamped-free condition in detail in this section. These boundary conditions are listed in Table 4.1.

Initial condition: We first assume that the acrosomal bundle is clamped at the wall and it has come to its initial deflection by a distributed constant load per unit length f by moving flow (See Fig. A-3). The deflection y, the displacement in the y direction of any point on the axis of the beam, can be then obtained by integrating the *load equation* $EIy'''' = f$ (also given in Eq. 4.3) four times with respect to x with appropriate boundary conditions from Table 4.2. The solution to the load equation

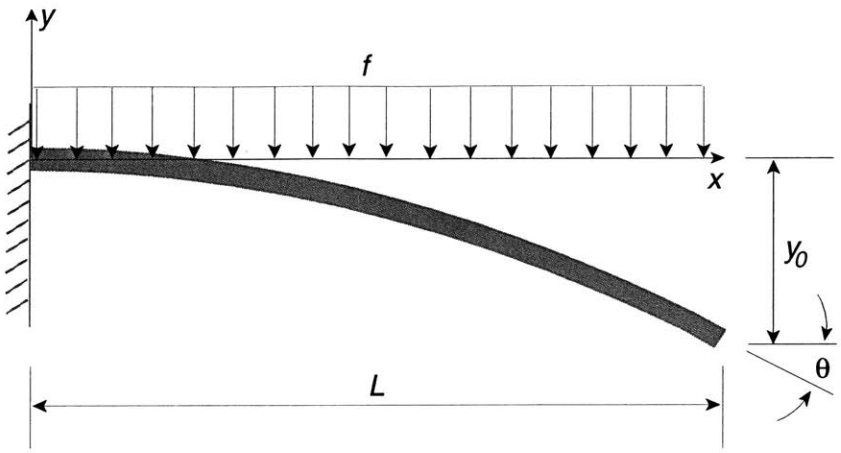

Figure A-3: A beam deflected by $y = y_0$ due to the presence of a constant load per unit length f. L is the length of the beam and θ is the angle between the deflected beam and the x-axis.

gives us the initial deflection in the actin bundle at $t = 0$, and takes the form:

$$y = \frac{fx^2}{24EI}(6L^2 - 4Lx + x^2) \tag{A.10}$$

where EI is the bending stiffness of the bundle, f is the constant load per unit length, and L is the length of the bundle. To a first approximation, we assume that the bundle has a uniform cross-sectional area, and EI can be treated as a constant. Since both EI and f are constants, we can set $C = f/EI$. Then, Eq. A.10 becomes $y = Cx^2(6L^2 - 4Lx + x^2)/24$ with only 1 unknown C which can be obtained by using

$$y(L, 0) = y_0 \tag{A.11}$$

where y_0 is the maximum initial deflection at $x = L$. Finally, our initial condition of the deflected beam takes the form:

$$y = \frac{y_0}{3}\left[\frac{6x^2}{L^2} - \frac{4x^3}{L^3} + \frac{x^4}{L^4}\right] \tag{A.12}$$

Clamped-Free boundary condition: At a clamped end (see Fig. A-4), $x = 0$, where there should be no displacement or slope allowed, the boundary conditions are

$$y(0, t) = 0$$

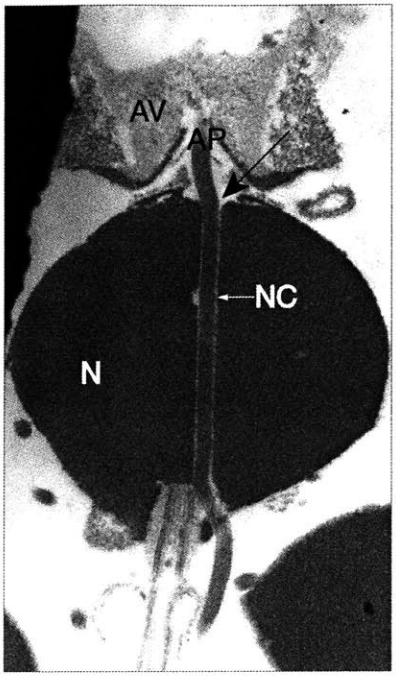

Figure A-4: An electron micrograph of a reacted sperm: The arrowhead locates the constrained boundary of the acrosomal process. The acrosome appears to be anchored in the nuclear channel. AP: acrosomal process, NC: nuclear channel, N: nucleus, AV: acrosomal vesicle.

$$\frac{\partial y(0,t)}{\partial x} = 0$$

while at $x = L$, the end is free with bending moment and shear force being equal to zero.

$$\begin{aligned} \frac{\partial^2 y(L,t)}{\partial x^2} &= 0 \\ \frac{\partial^3 y(L,t)}{\partial x^3} &= 0 \end{aligned} \tag{A.13}$$

A.1.5 Solution

By substituting the boundary conditions at $x = 0$ to Eq.(A.9), we obtain

$$c_1 = -c_3 \qquad \text{and} \qquad c_2 = -c_4. \tag{A.14}$$

When we use these and the boundary conditions at $x = L$, we obtain

$$c_1(cos\beta L + cosh\beta L) + c_2(sin\beta L + sinh\beta L) = 0$$

$$c_1(sin\beta L - sinh\beta L) - c_2(cos\beta L + cosh\beta L) = 0$$

which can be rewritten as

$$\begin{bmatrix} cos\beta L + cosh\beta L & sin\beta L + sinh\beta L \\ sin\beta L - sinh\beta L & -cos\beta L - cosh\beta L \end{bmatrix} \begin{pmatrix} c_1 \\ c_2 \end{pmatrix} = 0 \tag{A.15}$$

where the condition $\beta \neq 0$ has been used. In order for nonzero c_1 and c_2 to exist, the determinant of the coefficient matrix in Eq.(A.15) must vanish, giving us

$$cos(\beta L)cosh(\beta L) + 1 = 0. \tag{A.16}$$

There is an infinite number of solutions to Eq.(A.16), which can be designated as β_n $(n = 1, 2, 3, \ldots)$. β_n are the roots to the following equation and a few of those infinitely many values are given in Table A.3.

$$cos(\beta_n L)cosh(\beta_n L) + 1 = 0. \tag{A.17}$$

By substituting β_n into Eq. A.15, the ratio of c_{1n} and c_{2n} corresponding to β_n can be found as

$$\frac{c_{1n}}{c_{2n}} = \frac{sin\beta_n L + sinh\beta_n L}{-cos\beta_n L - cosh\beta_n L} = \frac{cos\beta_n L + cosh\beta_n L}{sin\beta_n L - sinh\beta_n L} \tag{A.18}$$

By combining Eq. A.9, A.14, and A.19, the eigenfunction $y_n(x,t)$ is given by

$$y_n(x,t) = \sum_{n=1}^{\infty} exp(-\frac{EI\beta_n^4 t}{\zeta}) c_{2n} \{sin\beta_n x - sinh\beta_n x - (cos\beta_n x - cosh\beta_n x)\frac{sin\beta_n L + sinh\beta_n L}{cos\beta_n L + cosh\beta_n L} \tag{A.19}$$

where c_{2n} can be found by applying an initial deflection y_0 at $x = L$ at $t = 0$ given in Eq. A.10. By substituting the initial condition and rearranging the solution, we obtain the final solution

Table A.3: A few values of β_n for Clamped-Free Boundary condition

Boundary conditions	Equation for β_n	β_ns
Clamped/Free	$cos(\beta_n L)cosh(\beta_n L) + 1 = 0$	$\beta_1 = 1.8751$ $\beta_2 = 4.6941$ $\beta_3 = 7.8548$

$$y_n(x,t) = \frac{y_0}{2}\, exp(-\frac{EI\beta_n^4 t}{\zeta})\cdot$$

$$\left\{\frac{(sin\beta_n x - sinh\beta_n x)(cos\beta_n L + cosh\beta_n L) - (cos\beta_n x - cosh\beta_n x)(sin\beta_n L + sinh\beta_n L)}{(sin\beta_n L\, cosh\beta_n L - sinh\beta_n L\, cos\beta_n L)}\right\} \tag{A.20}$$

A.1.6 Time constant to measure the bending stiffness

How long does it take for the initially bent rod to relax back to a straight conformation? As the initially bent rod, whose shape is represented by one of the solution modes, straightens out, it will maintain its shape but the amplitude of the bend will decrease exponentially as indicated in the solution, Eq. A.20. The exponential decaying time constant depends on the mode number $n = 1, 2, 3, ...$ and it is defined as

$$\tau_n = \frac{\zeta L^4}{EI\alpha_n^4} \tag{A.21}$$

where $\alpha_n = \beta_n L$ whose values are given in Table A.3.

What happens if the initial shape of the rod does not correspond to any of the modes found in our solution? In principle, any shape can be identified by superposing multiple hydrodynamic modes found in the solution. Therefore, just as in Fourier analysis in which any time-varying signal can be expressed as the sum of cosine and sine modes, we may superpose the relaxation of the constituent modes to obtain the relaxation dynamics of any arbitrarily bent rod [20]. Also, the time constant Eq. A.20 implies that as n increases, τ_n should decrease. In other words, the lower order modes relax more slowly than the higher order modes and thus the first mode, which

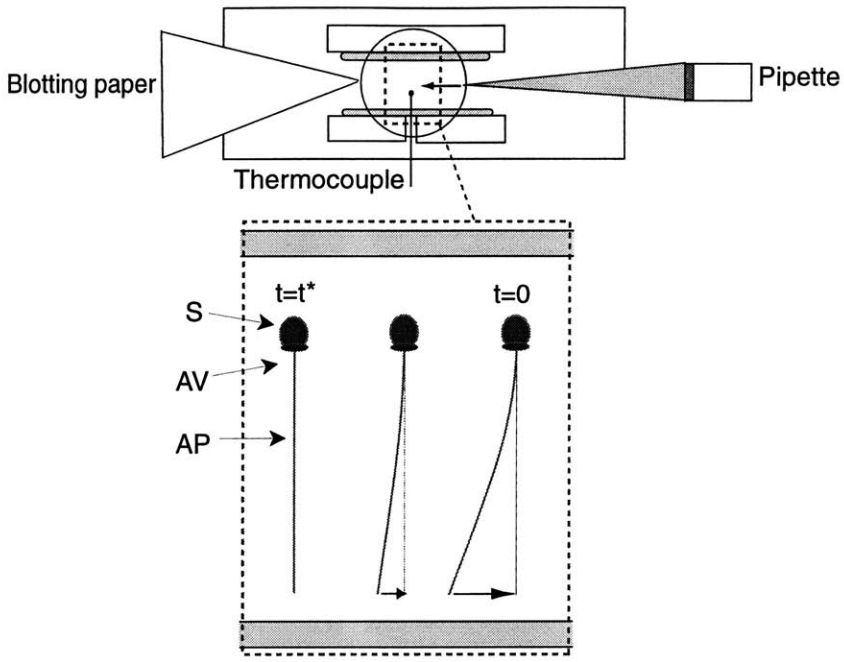

Figure A-5: A schematic of the decaying mode experiment using the hydrodynamic fluid flow in a flow channel: Once the sperms are settled at the bottom of the flow cell, a unidirectional flow is induced by injecting liquid from one side and simultaneously withdrawing it from the other side. When the acrosomal bundle is bent to the desired degree, the flow is stopped and the time of relaxation is measured. S: sperm head, AV: acrosomal vesicle, AP: acrosomal process. Size of the sperm is not drawn in scale.

is the longest, is the slowest mode. The lower order modes represent the rods of low stiffness and higher damping characteristic.

A.2 Experimental analysis

A.2.1 Experimental setup and sample preparation

We followed the same procedure as in 2.4.4. Briefly, 500μ sperms were collected from a selected crab, and the collected sperms were washed twice by centrifugation. The washed pellet was resuspended in ASW to its original volume, and kept on ice at all times.

All experiments are carried out with a flow channel whose both ends are left open for easy injection of buffer (See Fig. A-5). It has been observed that sperm heads,

when they are reacted, tend to get anchored on the surface of the coverslip, especially when the coverslips are treated with HCl to wash out impurities. Using the fact, we let the sperms settle down on the surface first by waiting for about 5 mins after injecting into the flow channel. Once they were settled down at the bottom of the flow channel, the calcium ionophore (A23187) dissolved in 95% ethanol was injected ($2mg/ml$ stock diluted 1:10 in 25mM $CaCl_2$ ASW).

When most of sperms were reacted, we searched for the anchored sperms lying perpendicular to the flow as indicated in Fig. A-5. By giving a gentle push on the microscope stage, I checked whether the acrosomal bundle was also glued to the surface by observing small motions of the tip of the bundle. We want the ones with their heads anchored on the surface with their acrosomal bundles being free in the fluid. 10 μl of sea water was then pippetted in from one end of the flow channel while the excess liquid was simultaneously being drawn with filter paper from the other end of the channel. This results in a fast flow inside the channel and the actin bundle bends along the flow. The filter paper was removed to stop the flow once the bundle was bent by a desired amount. The decaying motion was recorded until the actin bundle relaxed back to its straight resting position.

A.2.2 Light microscopy and data analysis

Image acquisition was done as described in the steady deflection mode experiment (See section 4.3.2). The images were then digitized using a Snapper frame grabber and a Openlab software (Improvision Inc.) at its rate of about 10 frames per second. Digitization with the Openlab timelapse generates time stamps for each frame and also features good quality enhancement options. The deflected distance of the tip from the resting state (the straight state) was measured for each frame using Openlab measurement, and the data were saved as an Excel file. Measured tip deflection was then plotted as a function of time using Matlab (The Math Works, Inc).

A.3 Results and discussions

A.3.1 Results

We have used hydrodynamic flow to bend the acrosomal bundles and derived their bending stiffness. Once the flow is stopped, the acrosomal bundle relaxes to its straight state and quantitative analysis of the decaying movement of the tip yields its bending stiffness. From Eq. A.20, we can obtain an expression for the deflection of the tip $x = L$ as a function of time, and it takes the form of

$$\frac{y_n(t)}{y_0} = e^{-t/\tau_n} \tag{A.22}$$

where τ_n is $\tau_n = \zeta L^4/EI\alpha_n^4$ (Eq. A.21). As shown in Fig. A-6, the initially deflected acrosomal bundle due to the flow is represented by the first mode ($n = 1$) solution to Eq. A.20 and Eq. A.22., and thus $\beta = \beta_1 = 1.8751$. By fitting a time series of the tip positions of the relaxing acrosomal bundle to the Eq. A.22 (with $n = 1$), its bending stiffness can be determined since every other quantity is known.

In this experimental setup, the sperms heads are anchored on the surface of the cover glass. Therefore, the acrosomal bundle extending out of the nucleus is also very close to the surface. I measured the distance between the surface of the coverslip and the acrosomal bundle by adjusting the focusing knob and reading off the increment. It was found that the acrosomal bundle is about 1-3μm away from the surface when their heads are glued on the surface. Consequently, ζ in this case is the drag coefficient of a cylinder moving perpendicular to its axis near a single plane wall, and its expression is given in Table. 4.1. μ is same as that of water since all the experiments were performed in ASW (artificial sea water). The length of the acrosomal bundle varied among individual cells from 46.2 to 57μm, and the initial tip displacement was between 8.4 and 20.4 μm. For all measurements, the initial deflection angle θ (See in Fig. A.4) was no greater than 0.41 radian (23.5°), which yields $sin\theta/\theta > 0.97$. This ensures that our analysis is valid since Eq. A.1 assumes a small angle θ.

Fig. A-7(a) shows time series of the decaying movement of an acrosomal bundle tip with a respective exponential fit to Eq. A.22. The bending stiffness can be

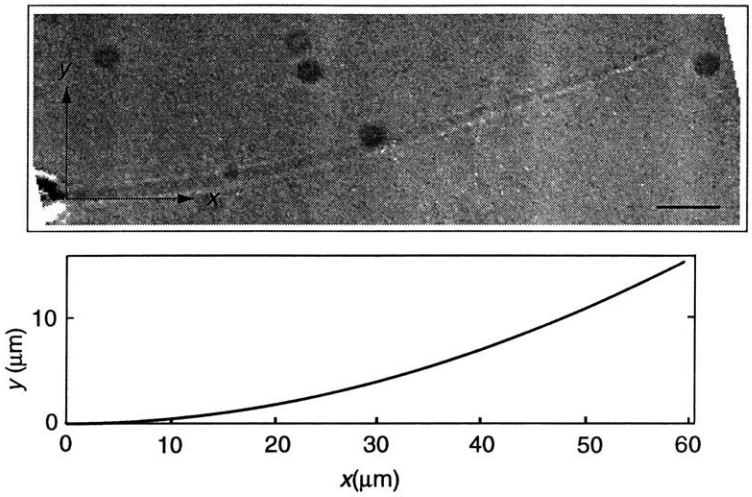

Figure A-6: Top: An image of the initially deflected acrosomal bundle by hydrodynamic flow. Bottom: The first mode solution from Eq. A.20 with values of L and y_0 measured from the image. The scale bar measures 5μm.

obtained directly from the fitted curve. For this particular acrosomal bundle, the bending stiffness was $EI \approx 1.1 \times 10^{-21}$.

As a second method, the quantity $\alpha_n^4 t/\zeta L^4$ can be replaced by a new variable τ^* to yield a new expression of Eq. A.22

$$\frac{y(t)}{y_0} = e^{-EI\tau^*}.$$

Fig.A-7(b) shows the results for the same acrosomal bundle as in Fig. A-7(a) in different axes. From this curve, one can determine the bending stiffness EI since it is the inverse of τ^* at the point where the decaying curve reaches $y(t)/y_0 = 1/e \approx 0.368$, which gives the same value of EI as the first method. The y-axis of the plot is normalized such that 1 and 0 correspond to the deflected and relaxed position, respectively. From measurements from 10 acrosomal bundle, we obtained the average value of the bending stiffness EI to be $1.66\times10^{-21}\text{Nm}^2$ with its standard deviation of $\pm0.5\times10^{-21}$.

A.3.2 Discussion

As one may notice from the times series plots in Fig. A-7(a) and (b), the theoretical curve deviates from the experimental data toward the end. The tip appears to relax

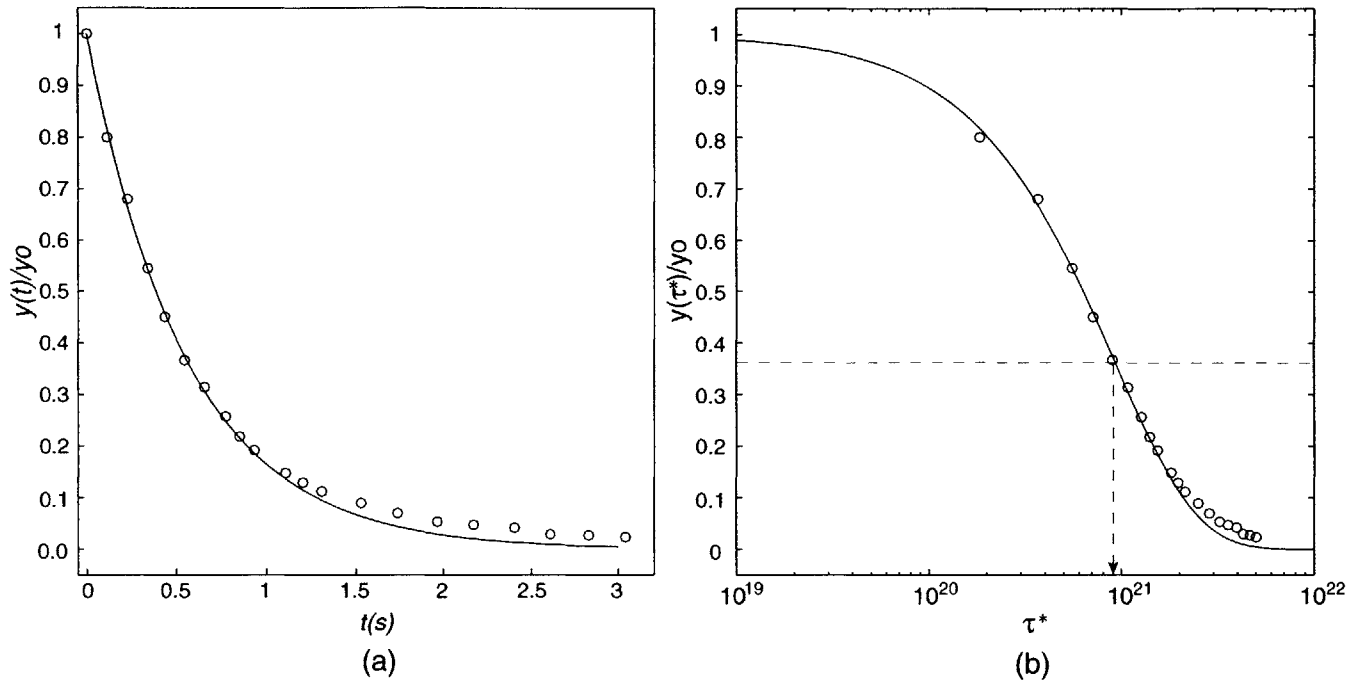

Figure A-7: (a) Time series of the tip of the acrosomal bundle relaxing from its initially deflected position y_0 to its resting position. The circles represent the experimental measurements, and the line is a fit to the expected exponential decay from Eq. A.22. (b) Time series of the same bundle as in (a) but in different axes. The bending stiffness EI can be determined directly by taking the inverse of τ^* at the point where the decaying curve reaches $y(t)$ $y_0 = 1/e \approx 0.368$. This particular bundle was 57μm long and its initial deflection was 30.4μm.

less than it should as the data points lie above the theoretical curve y/y_0 from Eq. A.22. We had a similar problem for all 10 of our data. Watching the movies of the relaxing acrosomal bundle carefully, we could visualize a residual flow by means of the presence of moving particles. Even if I suddenly stop the flow, it is likely that there remains residual fluid velocities that seem to complicate the interpretation of this experiment. When a flow that initially had a parabolic profile is suddenly stopped, there will be large negative velocities generated very close to the wall [45]. Therefore, exact effect of the flow during the bundle relaxation is not known and cannot be interpreted in the analysis at this point. Our estimation of the bending stiffness disregarding the residual flow offers the lowest order approximation.

Appendix B

Glossary

B.1 Biological terms [1]

Acrosome A membrane-bound compatment at the tip of the head of a sperm which contains lytic enzymes (hyaluronidase in mammalian sperm) that digest the outer surface of the egg and allow the sperm to inject its haploid DNA.

Actin A filamentous proteins (42 kD) involved in muscle contraction in both smooth and striated muscle and also serves as an important structural molecule for the cytoskeleton of many eukaryotic cells. It is the main constituent of the thin filaments of muscle fibers. The filaments (known also as filamentous or f-actin) can be dissociated into their globular subunits; each subunit is composed of a single polypeptide 375 amino acids long. This is known as globular or g-actin. In conjunction with myosin, actin is responsible for the contraction and relaxation of muscle.

ATP (adenosine triphosphate) A nucleotide present in all living cells which serves as an energy source for many metabolic processes and is required for ribonucleic acid synthesis.

Axoneme The central microtubule complex of eukaryotic cilia and flagella with the characteristic 9 + 2 arrangement of tubules when seen in cross-section.

Calcium An element taken in through the diet that is essential for a variety of bodily functions, such as neurotransmission, muscle contraction and proper heart function. Imbalances of calcium can lead to many health problems and excess calcium in nerve cells can

[1] Resources: (a) *On-line Medical Dictionary* (http://www.graylab.ac.uk/omd/index.html)
(b) *Life : the science of biology* by Purves et al., published by W.H. Freeman and Company in 1995

cause their death.

Calmodulin Ubiquitous and highly conserved calcium binding protein (17 kD) with four EF hand binding sites for calcium (3 in yeast). Ancestor of troponin C, leiotonin C and parvalbumin.

Cyst Any closed cavity or sac that is lined by epithelium often contains liquid or semi-solid material.

Flagellum In bacteria, a whiplike motility appendage present on the surface of some species. Flagella are composed of a protein called flagellin. Bacteria can have a single flagellum, a tuft at one pole, or multiple flagella covering the entire surface. In eukaryotes, flagella are threadlike protoplasmic extensions used to propel flagellates and sperm. Flagella have the same basic structure as cilia but are longer in proportion to the cell bearing them and present in much smaller numbers.

Limulus polyphemus Now renamed Xiphosura, though Limulus is still in common usage as a name. The king crab or horseshoe crab, found on the Atlantic coast of North America. It is more closely related to the arachnids than the crustacea and horseshoe crabs are the only surviving representatives of the subclass Xiphosura. Its compound eyes have been widely used in studies on visual systems, but it is probably better known from the Limulus amoebocyte lysate LAL) test, LAL is very sensitive to small amounts of endotoxin, clotting rapidly to form a gel and the test is used clinically to test for septicaemia.

Microtubule Cytoplasmic tubule, 25nm outside diameter with a 5nm thick wall. Made of tubulin heterodimers packed in a three start helix (or of 13 protofilaments looked at another way) and associated with various other proteins (MAPs, dynein, kinesin). Microtubules of the ciliary axoneme are more permanent than cytoplasmic and spindle microtubules.

Myosin A family of motor ATPases that interact with F actin filaments. An increasing number of different myosins are being described. Myosin I is a low molecular weight (111-128 kD) form found in protozoa Acanthamoeba and Dictyostelium) that does not self assemble and is found in the cytoplasm as a globular monomeric molecule that can associate with membranes and transport membrane vesicles along microfilaments.

Brush border Myosin I is a single headed myosin found in the microvilli of ver-

tebrate intestinal epithelial cells, linking the membrane to the microfilament core. There is a single heavy chain of 119 kD and multiple (3 or 4) calmodulin light chains. The heavy chain has a C terminal domain that binds to acidic phospholipids.

Myosin II is the classical sarcomeric myosin that self assembles into bipolar thick filaments. Myosin II is a multimeric protein (440 kD) with two heavy chains (200 kD) and two pairs of light chains (17-22 kD) in each hexamer.

Between species and tissues there are considerable variations in the properties of Myosin II (see myosin light chains, meromyosin). Cytoplasmic myosin II is a family of sarcomeric myosin like proteins, also hexameric, responsible for force generation by interaction with microfilaments.

There are two heavy chains (up to 240 kD) and two pairs of light chains (15-20 kD), the self assembled filaments are shorter than those of the sarcomere. The MYO2 gene product is an unconventional myosin from yeast involved in polarized secretion. MYO2 may be similar to dilute myosin from mouse and p190 protein from vertebrate brain.

Scallop myosin is directly calcium regulated (through regulatory and essential light chains) and is more similar to sarcomeric myosin than to the nonsarcomeric myosins. Smooth muscle myosin has two 200 kD heavy chains, two regulatory 20 kD light chains that can be phosphorylated, altering its binding to the heavy chains which induces a conformational change that renders the myosin active and two 17 kD light chains.

Scruin Actin binding protein found associated with the acrosomal process of Limulus polyphemus. Scruin holds the microfilaments of the core process in a strained configuration so that the process is coiled. The myosin binding sites on the microfilaments are blocked so HMM decoration is impossible, indicating that there is an unusual packing conformation, when the scruin actin binding is released the process straightens, the conformation of the actin changes and myosin binding is possible.

B.2 Chemical terms

Buffer A system that acts to minimise the change in concentration of a specific chemical species in solution against addition or depletion of this species. PH buffers: weak acids or weak bases in aqueous solution. The working range is given by pKa +/ 1. Metal ion buffers: a metal ion chelator for example EDTA, partially saturated by the metal ion acts, as a buffer for the metal ion.

EGTA (egtazic acid) A chelating agent relatively more specific for calcium and less toxic than edetic acid (edta). It has been used in the treatment of urolithiasis. Pharmacological action: antidotes, chelating agents.

Ionophore A molecule that allows ions to cross lipid bilayers. There are two classes: carriers and channels. Carriers, like valinomycin, form cage like structures around specific ions, diffusing freely through the hydrophobic regions of the bilayer. Channels, like gramicidin, form continuous aqueous pores through the bilayer, allowing ions to diffuse through.

Triton X-100 Nonionic detergent used in isolating membrane proteins: the detergent replaces the phospholipids that normally surround such a protein. Other detergents of the Triton group are occasionally used so the full name should be quoted.

B.3 Physical terms [2]

Bending moment (M) The first moment of stress integrated over any cross section of a structural member, equal to the algebraic sum of the moments of all forces to either side of the section; the moment is about the sectional neutral axis along which the bending stress is equal to sectional mean bending stress; a positive bending moment bends the beam convex downward, while a negative one bends the beam convex upward. Dimension[3]: ML^2T^{-2}

Bending stiffness (EI) This is also called *flexural rigidity* and represents a measure of the resistance of a beam to bending. The larger the flexural rigidity is, the smaller the curvature for a given bending moment. Dimension: ML^3T^{-2}

Crystalline the state of a solid material characterized by a periodic and repeating three-dimensional array of atoms, ions, or molecules.

[2]Resource: *Mechanics of Materials* by Gere and Timoshenko, published in 1997 by PWS publishing company

[3]$M, L, T, and \Theta$ represent mass, length, time and temperature, respectively.

Density (ρ) A physical property of fluids defined by the ratio of the mass of fluid in a fluid element to its volume. $\rho = m/V$ where m is the mass and V is the volume of the fluid. Dimension [4]: ML^{-3}

Drag force ($\mathbf{f}_{drag}$) a force (per unit length) that opposes an object moving through a fluid. Dimension: MT^{-2}

Drag coefficient (ζ) defined by f_{drag}/v where v is the velocity of the object. Dimension: $ML^{-1}T^{-1}$

Elastic potential energy the energy made available for use by the return of an elastic body to its original configuration. Dimension: ML^2T^{-2}

Moment of Inertia (I) The tendency of a body rotating about a fixed axis to resist a change in this rotating motion, expressed as the integral over the body's volume of its density, multiplied by the square of the distance to the axis. $I_x = \int y^2 dA$ or $I_y = \int x^2 dA$. Dimension: L^4

Viscosity (μ) A physical property of fluids that determines the the internal friction of a fluid; the resistance to flow exhibited by a liquid or gas subjected to deformation; viscosity is expressed by a coefficient, in units of poise (1 poise = 0.1 Pa-sec). Kinematic viscosity is defined as μ/ρ where ρ is the density. Dimension: $ML^{-1}T^{-1}$

Young's modulus (E) The ratio between tensile or compressive stress (σ) and elongation (ϵ) of a solid stressed in one direction. Dimension: $ML^{-1}T^{-2}$

Viscous dissipation rate ($\dot{E}$) The rate of energy dissipated due to viscosity of the medium. Dimension: ML^2T^{-3}

[4] $M, L, T, and \Theta$ represent mass, length, time and temperature, respectively.

Bibliography

[1] J. Andrè. A propos d'une lecon sur la limule. *Ann. Fac. Sci. Univ. Clermont*, 26:27–38, 1965.

[2] B. Baccetti. The biology of the sperm cell. *Monogr. Dev. Biol.*, 10:1–254, 1976.

[3] D. Bray. *Cell Movements.* Garland Publishing, INC, 1992.

[4] G. G. Brown. Scanning electron-microscopical and other observations of sperm fertilization reactions in *limulus polyphemus* (merostomata: Xiphosura). *J. Cell. Sci.*, 22(3):547–562, 1976.

[5] R.G. Cox. The motion of long slender bodies in a viscous fluid part 1. general theory. *J. Fluid Mech.*, 44(4):791–810, 1970.

[6] R.G. Cox. The motion of long slender bodies in a viscous fluid part 2. shear flow. *J. Fluid Mech.*, 45(4):625–657, 1971.

[7] J. C. Dan. Morphogenetic aspects of acrosome formation and reaction. *Adv. Morpho.*, 8:1–39, 1970.

[8] D. DeRosier. How actin filaments pack into bundles. *Cold Spring Harb Symp. Quant. Biol.*, 46:525–540, 1982.

[9] D. DeRosier. How to build a bend into an actin bundle. *J. Mol. Biol.*, 175:57–73, 1984.

[10] D. DeRosier, L. Tilney, and P. Flicker. A change in the twist of the actin-containing filaments occurs during the extension of the acorosomal process in *limulus* sperm. *J. Mol. Biol.*, 137:375–389, 1980.

[11] D. DeRosier, L. G. Tilney, E. M. Bonder, and P. Frankl. A change in twist of actin provides the force for the extension of the acrosomal process in limulus sperm: the false-discharge reaction. *J. Cell Biol.*, 93(2):324–37, 1982.

[12] E. H. Egelman and D. J. DeRosier. Image analysis shows that variations in actin crossover spacings are random, not compensatory. *Biophys. J.*, 65(5):1299–1305, 1992.

[13] E. H. Egelman, N. Francis, and D. J. DeRosier. F-actin is a helix with a random variable twist. *Nature*, 298:131–135, 1982.

[14] W.H. Fahrenbach. Spermiogenesis in the horseshoe crab, *limulus polyphemus. J. Morphol.*, 140:31–52, 1973.

[15] H. Felgner, R. Frank, and M. Schliwa. Flexural rigidity of microtubules measured with the use of optical tweezers. *J. Cell Sci.*, 109:509–16, 1996.

[16] R. Feynman. *The Feynman lectures on physics.* Addison-Wesley Publishing Company, INC, 1963.

[17] D.K. Fygenson. *Microtubules: The rythm of assembly and the evolution of form.* PhD thesis, Princeton University, 1995.

[18] F. Gittes, B. Mickey, J. Nettleton, and J. Howard. Flexural rigidity of microtubules and actin filaments measured from thermal fluctuations in shape. *J. Cell Biol.*, 120(4):923–934, 1993.

[19] M. F. Gluch, D. Typke, and W. Baumeister. Motility and thermotactic response of *thermotoga maritima. J. Bacteriol.*, 177(19):5473–5479, 1995.

[20] J. Howard. *Protein Machines: The mechanics of motor proteins and the cytoskeleton, Part I: Physical principles.* University of Washington, 1998.

[21] A. J. Hunt, F. Gittes, and J. Howard. The force exerted by a single kinesin molecule against a viscous load. *Biophys. J.*, 67:766–781, 1994.

[22] B.L. Hylander and R.G. Summers. An ultrastructural analysis of the gametes and early fertilization in two bivalve molluscs, chama macerophylla and spisula solidissima with special reference to gamete binding. *Cell. Tissue Res.*, 182(4):469–489, 1977.

[23] H. Brenner J. Happel. *Low Reynolds Number Hydrodynamics.* Prentice-Hall, Inc, 1965.

[24] D.J. Jeffrey and Y. Onishi. The slow motion of a cylinder next to a plane wall. *Quant. J. Mech. Appl. Math*, 34:129–137, 1981.

[25] H. Jessen. Actin-like filaments in the acrosomal apparatus of spermatozoa of a sea urchin. *Exp. Cell. Res.*, 80:47–54, 1973.

[26] R. Kamiya, H. Hotani, and S. Asakura. Polymorphoc transition in bacterial flagella. *Symp Soc Exp Biol*, 35:53–76, 1982.

[27] C. H. Keller, B. B. Olwin, D. C. LaPorte, and D. R. Storm. Determination of the free-energy coupling for binding of calcium ions and troponin i to calmodulin. *Biochem*, 21:156–162, 1982.

[28] J. B. Keller and S. I. Rubinow. Swimming of flagellated microorganisms. *Biophys. J.*, 16:151–170, 1976.

[29] H. Lamb. *Hydrodynamics.* Dover Publication, 1932.

[30] L.D. Landau and E.M. Lifshitz. *Theory of Elasticity, 3rd ed.* Pergamon, Inc, 1986.

[31] H. Larson. *Introduction to probability.* Addison-Wesley, 1994.

[32] K.E. Machin. Wave propagation in flagella. *J. Exp. Biol*, 35:796–807, 1958.

[33] L. Mahadevan and P. Matsudaira. Motility powered by supramolecular springs and ratchets. *Science*, 288(5463):95–100, 2000.

[34] L. Mahadevan, J.H. Shin, and P. Matsudaira. Energy of an actin spring. preprint, 1999.

[35] H. Miyata and H. Hotani. Morphological changes in liposomes caused by polymerization of encapsulated actin and spontaneous formation of actin bundles. *Proc. Natl. Acad. Sci. USA*, 89:11547–11551, 1992.

[36] F.R.N. Nabarro. *Theory of crystal dislocations.* Dover Publication, 1993.

[37] By the courtesy of Nicki Watson. *Whitehead Institute, Cambridge, MA 02139, USA.*

[38] L. Niijima and J. Dan. The acrosome reaction in *mytilus edulis.* 1. fine structure of the intact acrosome. *J. Cell Biol.*, 25:243, 1965.

[39] B. B. Olwin, A. M. Edelman, E. G. Krebs, and D. R. Storm. Quantitation of energy coupling between ca^{2+}, calmodulin, skeletal muscle myosin light chain kinase, and kinase substrates. *J. Biol. Chem*, 259:10949–10955, 1984.

[40] B. B. Olwin and D. R. Storm. Ca^{2+} binding to complexes of calmodulin and calmodulin binding proteins. *Biochem*, 24:8081–8086, 1985.

[41] F. Oosawa and S. Asakura. *Thermodynamics of the polymerization of protein.* Academic Press, Inc, 1975.

[42] A. Pijper and G. Abraham. Wavelengths of bacterial flagella. *J. Gen. Microb.*, 10:452–456, 1954.

[43] J.D. Potter, P. Strang-Brown, P.L. Walker, and S Iida. Ca^{2+} binding to calmodulin. In *Methods in Enzymology*, volume 102, chapter 12. Academic Press, Inc, 1983.

[44] D. Riveline, C.H. Wiggins, R.R. Goldstein, and A. Ott. Elastohydrodynamic study of actin filaments using fluorescence microscopy. *Phys. Rev. E*, 56(2):R1330–1333, 1997.

[45] I thank Professor Roger Kamm for communication on this subject. *Department of Mechanical Engineering, MIT, Cambridge, MA 02139.*

[46] M. C. Sanders, M. Way, J. Sakai, and P. Matsudaira. Characterization of the actin cross-linking properties of the scruin- calmodulin complex from the acrosomal process of limulus sperm. *J. Biol. Chem.*, 271:2651–7, 1996.

[47] P. Seller, J. Laynex, E. Thulin, and S. Forsen. Thermodynamics of ca^{2+} binding to calmodulin and its tryptic fragments. *Biophy. Chem*, 39:199–204, 1991.

[48] M. B. Sherman, J. Jakana, S. Sun, P. Matsudaira, W. Chiu, and M. F. Schmid. The three-dimensional structure of the limulus acrosomal process: a dynamic actin bundle. *J. Mol. Biol*, 294(1):139–49, 1999.

[49] R.B. Stein, T. Gordon, and J. Shriver. Temperature dependece of mammalian muscle contractions and atpase activities. *Biophys. J.*, 40:97–107, 1982.

[50] Y. Takaisi. The drag on a circular cylinder moving with low speeds in a viscous liquid between two parallel walls. *J. Phys. Soc. Japan*, 10:685–693, 1955.

[51] Y. Takaisi. Note on the drag on a circular cylinder moving with low speeds in a semi-infinite viscous liquid bounded by a plane wall. *J. Phys. Soc. Japan*, 11:1004–1008, 1956.

[52] L. G. Tilney. Actin filaments in the acrosomal reaction of limulus sperm. motion generated by alterations in the packing of the filaments. *J. Cell Biol*, 64(2):289–310, 1975.

[53] L. G. Tilney. The acrosomal reaction. In *Biology of Fertilization*, volume 2, chapter 5. Academic Press, Inc, 1985.

[54] L. G. Tilney, Y. Fukui, and D. DeRosier. Movement of the actin filament bundle in *mytilus* sperm: A new mechanism is proposed. *J. Cell Biol.*, 104:981–993, 1987.

[55] L.G. Tilney, E.M. Bonder, and D.J. DeRosier. Actin filaments elongate from their membrane-associated ends. *J. Cell Biol*, 90:485–494, 1981.

[56] M.M. Tirado and J. Carcia de la Torre. Translational friction coefficients of rigid, symmetric top macromolecules. application to circular cylinders. *J. Chem. Phys.*, 71:2581–2587, 1979.

[57] M.M. Tirado and J. Carcia de la Torre. Rotational dynamics of rigid, symmetric top macromolecules. application to circular cylinders. *J. Chem. Phys.*, 73:1986–1993, 1980.

[58] P. Venier, A. C. Maggs, M. F. Carlier, and D. Pantaloni. Analysis of microtubule rigidity using hydrodynamic flow and thermal fluctuations [published erratum appears in j biol chem 1995 jul 14;270(28):17056]. *J. Biol. Chem.*, 269(18):13353–60, 1998.

[59] C. H. Wiggins, D. Riveline, A. Ott, and R. E. Goldstein. Trapping and wiggling: elastohydrodynamics of driven microfilaments. *Biophys. J.*, 74(2):1043–60, 1998.